SCISPACE
formerly Typeset

Open access • Posted Content • DOI:10.1021/JACSAU.1C00276

Quantifying the Impact of Parametric Uncertainty on Automatic Mechanism Generation for CO2 Hydrogenation on Ni(111). — Source link

Bjarne Kreitz, Bjarne Kreitz, Khachik Sargsyan, Katrin Blondal ...+5 more authors

Institutions: Brown University, Clausthal University of Technology, Sandia National Laboratories, Northeastern University

Published on: 16 Aug 2021 - ChemRxiv (American Chemical Society (ACS))

Topics: Parametric statistics

Related papers:

- To address surface reaction network complexity using scaling relations machine learning and DFT calculations
- Uncertainty quantification, propagation and characterization by Bayesian analysis combined with global sensitivity analysis applied to dynamical intracellular pathway models.
- Quantitative Evaluation of the Effect of Uncertainty in Property Models on the Simulated Performance of Solvent-Based CO2-Capture☆
- A Comparison of Methods for Quantifying Prediction Uncertainty in Systems Biology
- Uncertainty analyses for Ecological Network Analysis enable stronger inferences

Share this paper:

View more about this paper here: https://typeset.io/papers/quantifying-the-impact-of-parametric-uncertainty-on-2ifdkn9z4k

Quantifying the Impact of Parametric Uncertainty on Automatic Mechanism Generation for CO_2 Hydrogenation on Ni(111)

Bjarne Kreitz,[*,†,‡] Khachik Sargsyan,[¶] Emily J. Mazeau,[§] Katrín Blöndal,[‡] Richard H. West,[§] Gregor D. Wehinger,[†] Thomas Turek,[†] and C. Franklin Goldsmith[*,‡]

†*Institute of Chemical and Electrochemical Process Engineering, Clausthal University of Technology, Clausthal-Zellerfeld, Germany*
‡*School of Engineering, Brown University, Providence, RI, USA*
¶*Sandia National Laboratories, Livermore, CA 94550, USA*
§*Department of Chemical Engineering, Northeastern University, Boston, MA 02115, USA*

E-mail: kreitz@icvt.tu-clausthal.de(BK); franklin_goldsmith@brown.edu(CFG)
Phone: +49 5323 72 2473 (BK); +1 401 863 6468 (CFG)

Abstract

Automatic mechanism generation is used to determine mechanisms for the CO_2 hydrogenation on Ni(111) in a two-stage process, while considering the uncertainty in energetic parameters systematically. In a coarse stage, all the possible chemistry is explored with gas-phase products down to the ppb level, while a refined stage discovers the core methanation submechanism. 5,000 unique mechanisms were generated, which contain minor perturbations in all parameters. Global uncertainty assessment, global sensitivity analysis, and degree of rate control analysis are performed to study the effect of this parametric uncertainty on the microkinetic model predictions. Comparison of the model predictions with experimental data on a Ni/SiO_2 catalyst find a feasible set of microkinetic mechanisms that are in quantitative agreement with the measured data, without relying on explicit parameter optimization. Global uncertainty and sensitivity analyses provide tools to determine the pathways and key factors that control the methanation activity within the parameter space. Together, these methods reveal that the degree of rate control approach can be misleading if parametric uncertainty is not considered. The procedure of considering uncertainties in the automated mechanism generation is not unique to CO_2 methanation and can be easily extended to other challenging heterogeneously catalyzed reactions.

Methanation is a promising technology for reducing CO_2 emissions while producing sustainable natural gas. From a climate-change perspective, the process is particularly advantageous when excess renewable energy is used to generate the requisite H_2 via water splitting as part of the Power-to-Gas process.[1,2] However, volatility in renewable energy sources induces challenges on the transient operation of a catalytic reactor.[3] Given that the net reaction, $CO_2 + 4\,H_2 \rightleftharpoons CH_4 + 2\,H_2O$, is exothermic, $\Delta H_{\mathrm{rxn}}\,(298\,\mathrm{K}) = -164.7\,\mathrm{kJ\,mol^{-1}}$, transient operation can lead to undesirable temperature and concentration gradients.[4–6] Accordingly, an accurate microkinetic mechanism is essential for optimizing reactor performance.

The most commonly used methanation catalyst is Ni, due to its good performance at reasonable costs.[2,7] Ni(111) has the highest share on a Ni crystal,[8] yet its role in CO_2 methanation is unresolved, despite extensive research.[9–17] Experiments with Ni/γ-Al_2O_3 catalysts point to the higher activity of Ni(111) terrace sites, whereas experiments on Ni/SiO_2 show a higher activity of Ni(211) steps, which are also considered to be the active site for CO methanation.[18] Lozano et al.[12] combined density functional theory (DFT) calculations using the BEEF-vdW functional and kinetic Monte Carlo simulations to demonstrate that the Ni(111) surface is inactive for the CO_2 methanation; instead, they argued that the catalyst converts the CO_2 to CO in the reverse water-gas shift (RWGS) reaction, $CO_2 + H_2 \rightleftharpoons CO + H_2O$, with the CO_2^* dissociation being the rate-determining step (RDS). In the study of Vogt et al.,[10] the four most dominant Ni facets were investigated by DFT with the PBE functional. They showed in a mean-field microkinetic model that although the Ni(111) facet is not as active as the open (110) facet, it still exhibited some methanation activity. These authors identified the dissociation of HCO^* as the RDS, which is supported by Zhou et al.[15] from DFT calculations with the same functional. In addition to these models of CO_2 hydrogenation on Ni(111), other studies focused on the (reverse) water-gas shift reaction,[19–21] methanol synthesis,[22] and formic acid formation.[23] Apart from the general role/activity of the Ni(111) facet, the dominant reaction network for CO_2 hydrogenation has not been conclusively determined; the aforementioned computational studies disagree about important intermediates, pathways, and the RDS.

The microkinetic mechanism for CO_2 hydrogenation on Ni(111) can be developed based either on surface science experiments assisted by operando methods,[9,10,13,24] or by computational methods (*e.g.* DFT).[16,19,25–28] DFT-based microkinetic mechanisms are increasingly common, due to the availability of "black-box" electronic structure codes. Although modern DFT functionals are reliable for adsorbate thermochemistry and kinetics, these calculations remain computationally expensive. Accordingly, given a computational "budget", researchers must prioritize which intermediates and transition states to investigate. This process assumes that the researcher knows *a priori* which intermediates and transition states will be important. Consequently, the mechanism generation process can be biased by the developer's expectations.[29,30] An alternative to DFT-based mechanism development is to use approximate methods that, while less accurate, are orders of magnitude faster. One such method is applying linear scaling (LS) relations, which are based on the d-band model.[31] LS relations can accelerate the procedure,[32] and are often used for catalyst screening.[28,33,34] Although these approximate methods save computational resources, they still require expertise and intuition to develop the mechanism, and this procedure does not avoid the problem of incompleteness due to bias. An alternative to constructing mechanisms "by hand" is to use computers to propose and evaluate possible elementary reactions.[35–42] One such approach is the automatic Reaction Mechanism Generator (RMG) of Green and coworkers.[39,43] Originally developed for gas-phase pyrolysis, RMG has been expanded to include reactions on surfaces.[40–42]

The omission (intentional or unintentional) of certain reactions can be characterized as mechanistic uncertainty. In addition to bias, a second problem with microkinetic mechanism generation is parametric uncertainty. All of the DFT-derived parameters carry uncertainties because of the assumptions made in the exchange-correlation functional. For example, the binding energies are assumed to have an uncertainty of $\pm\ 0.3\,\mathrm{eV}$.[44] However, the uncertainties in binding energies for different adsorbates are correlated[45–47] (indeed, some degree of correlation is implicit in LS, and the BEEF-vdW functional exploits this correlation[48,49]). In addition to correlation among adsorbate thermochemistry, reaction kinetics are correlated as well, as exemplified by Brønsted-Evans-Polanyi (BEP) relations.[50] The uncertainty in model parameters should be propagated to the outputs of the model, *e.g.* conversion, turnover frequency (TOF)[44,45,49,51] and to identify the path with the highest occurring frequencies in a mechanism.[51–53] However, given the large uncertainty in model parameters, some pathways or intermediates might have been overlooked because of the very complex landscape of the potential energy surface.[30] Therefore, it is necessary to account for the uncertainty directly in the mechanism generation procedure to provide an exhaustive analysis of all possible reactions and intermediates.

The present work aims to combine experiment, theory, and modeling to develop a microkinetic model for the hydrogenation of CO_2 on Ni(111). Instead of propagating uncertainty from a final microkinetic model to the simulation outputs, we take a novel approach and include the uncertainty directly in the mechanism generation procedure in RMG. The automatic mechanism generation process is repeated 5,000 times, with each new mechanism including small perturbations in the DFT-derived parameters that can also result in mechanisms with different species and reactions. Therefore, we can discover all possible reactions and intermediates in a vast reaction network. Global sensitivity analysis (GSA) and local sensitivity analysis using the degree of rate control (DRC) are used to identify the most important species and reactions over the whole uncertainty range. The mechanisms are compared against experimental data for a Ni/SiO_2 catalyst in a differential fixed-bed reactor. This comparison determines a feasible set of microkinetic mechanisms that quantitatively agree with the experimental data. Combining all of the methods allows us to advance our understanding of the factors controlling the methanation activity on Ni(111) and to derive a most likely methanation mechanism. Applying the DRC on each unique mechanisms shows how versatile the DRC can be in a confined uncertainty range and how much more information on the controlling factors is obtained when global uncertainty is considered. This study provides an example for the benefit of automated mechanism generation and the consideration of uncertainties to discover all the possible chemistry.

Materials and Methods

Microkinetic Mechanism Generation

Automated mechanism generation was performed with RMG (version 3.0).[43,54] A detailed explanation of the RMG software can be found in the work of Gao et al.[39] and the extension to heterogeneously catalyzed reactions in the publication from Goldsmith and West.[40] Only a brief explanation of the key features important for this work is provided. Elementary reactions are grouped according to reaction families, which are templates that convert the chemical graphs of reactants into products. For each proposed species and elementary reaction, RMG must provide thermodynamic properties and a rate coefficient, respectively. RMG combines a database of precompiled values, but it can supplement these databases with rules for predicting the properties for novel species/reactions. The total species population is divided into two groups: core and edge. Core species are essential to the mechanism;

typically, at the start of the process, only the reactants are contained in the core. The species in the core are iterated through the reaction families, which potentially will generate new species. RMG uses a rate-based algorithm to expand the mechanism.[39,55] When RMG proposes a new species, that species starts off in the edge. If the net rate of production of that edge species is sufficiently large (based upon user-defined criteria), then it is moved from the edge to the core, and the process begins anew. Thus, RMG exhaustively considers all possible reactions that are consistent with the various reaction families for the core species; however, it only retains the species that are kinetically relevant for the conditions of interest.

The automated mechanism generation requires that RMG predicts the thermochemistry of adsorbates and the kinetics for the elementary reactions. Thermodynamic properties of the adsorbates on the Ni facet were estimated via LS relations[31] (see Equation (1)), which were recently implemented in RMG by Mazeau et al.,[41] based on reference values for Pt(111) obtained via BEEF-vdW calculations in Ref. 42. The binding energy of an adsorbate is estimated via:

$$\Delta E_{\mathrm{Ni}}^{\mathrm{AX}} = \Delta E_{\mathrm{Pt}}^{\mathrm{AX}} + \gamma \left(\Delta E_{\mathrm{Ni}}^{\mathrm{A}} - \Delta E_{\mathrm{Pt}}^{\mathrm{A}}\right) \tag{1}$$

where $\Delta E_{\mathrm{Pt}}^{\mathrm{AX}}$ is the binding energy of the adsorbate AX^* in the Pt(111) database, where X represents any adsorbate, $\Delta E_{\mathrm{Ni}}^{\mathrm{A}}$ is the binding energy of the adatom A^* through which AX^* binds on Ni(111), $\Delta E_{\mathrm{Pt}}^{\mathrm{A}}$ is the analogous property for Pt(111), and the slope γ is related to the degree of saturation for the adsorbate. Accordingly, RMG requires values for $\Delta E_{\mathrm{Ni}}^{\mathrm{H}}$, $\Delta E_{\mathrm{Ni}}^{\mathrm{C}}$, and $\Delta E_{\mathrm{Ni}}^{\mathrm{O}}$ for the Ni(111) facet for use in the LS procedure. These values were obtained from DFT calculations.[8] Additionally, the Pt(111) database in Ref. 42 only considered adsorbates with no more than two heavy atoms (C, N, and O); RMG can use those values to estimate the thermodynamic properties of larger adsorbates.[56] However, we anticipated that three adsorbates – CO_2^*, HCOO^*, and COOH^* – would be essential to the model, and so new DFT values were added to the Pt(111) database. DFT calculations were performed using the RPBE[57] functional in VASP[58,59] with dispersion correction[60] and converted to thermodynamic properties of the adsorbates as described in Ref 42. A detailed description of the DFT method is provided in the Supporting Information (SI).

As mentioned above, elementary reactions are provided in the form of templates for a certain reaction family. Kinetic parameters typically are provided as an Arrhenius fit, $k(T) = A\exp(-E_\mathrm{a}/RT)$, where A is the pre-exponential factor, E_a is the activation energy, and R is the ideal gas constant. RMG estimates only kinetic parameters in one direction (*e.g.* forward); the reverse rate constant is computed from the equilibrium constant, which ensures thermodynamic consistency. In the present study, we assumed that CO_2 and H_2O adsorb associatively.[9,12,20] CH_4, in contrast, has two possible adsorption pathways: association to a physisorbed precursor state CH_4^* (which can then go on to dissociate on the surface),[61] and direct dissociative adsorption to CH_3^* and H^*.[9,12]

RMG includes several libraries of rate constants taken from values reported in the literature or computed via DFT. However, for the purposes of the present work, all the rate constants were estimated using BEP relations, with one exception, the CO_2 dissociation. Due to the comparatively unique structure of CO_2^*, the activation energy for CO_2^* dissociation is not well described by the general BEP relation for cleavage a C=O bond on a surface and was, therefore, included as a specific reaction in a library based on previous work.[8] By eliminating the reaction libraries in favor of the BEP relations, we can systematically quantify the effects of correlated uncertainty in thermodynamic properties (*e.g.* heats of formation) on rate constants and vary all reactions within a given reaction family. Accordingly, the activation energy for surface reactions is estimated using a BEP relation specific for that reaction family:

$$E_\mathrm{a} = E_\mathrm{a}^0 + \alpha\,\Delta H_\mathrm{rxn} \tag{2}$$

where the intercept E_a^0 is the characteristic activation energy of a reaction family, and α is the dimensionless slope of the BEP, so that the activation energy scales with the heat of reaction, ΔH_{rxn}. BEP relations are organized in a tree structure with the most general relation at the top (*e.g.* generic bond fission) and more specific child nodes beneath (*e.g.* C-C bond fission). RMG climbs down the tree to the most specific node available to estimate kinetic parameters.

The present work builds upon the pre-existing reaction families for surface kinetics,[40,41] which can be categorized into adsorption/desorption, bond fission, and abstraction. All of the existing BEP values were updated based upon new DFT calculations or literature data. In particular, new values were added for the abstraction families (see SI for details). The overwhelming majority of microkinetic mechanisms consist of only adsorption/desorption and bond fission reactions; the inclusion of bimolecular-to-bimolecular reactions, such as abstraction, have been primarily neglected[29,30] but can become important, especially at high coverage conditions.[62] As will be demonstrated in the results section, these abstraction reactions can contribute significantly to the overall reactivity of the system. The rate constants were computing using transition state theory, with the saddle points obtained via climbing-image nudged elastic band (CINEB) method[63] (see SI for further details). A complete summary of the reaction families, including the BEP relations used for the mechanism generation procedure, is provided in Table S1 and Figures S1 to S10. The initial conditions of the mechanism generation process were set to a stoichiometric H_2/CO_2 mixture, with a vacant Ni(111) surface, at temperatures of 573 K and 673 K, and a pressure of 1 bar. Further parameters and settings used for the generation procedure are summarized in Table S2.

Experiments

CO_2 methanation experiments were conducted with a 20 wt% Ni/SiO_2 catalyst produced with a spray-drying method as described in the work of Kreitz et al.[64] A solution of colloidal SiO_2 nanoparticles with a primary particle size of 8 nm and $Ni(NO_3)_2$ was sprayed into a tubular furnace operated at 673 K using an atomizer to initiate a one-step calcination and assembly of Ni/SiO_2 nanoparticles. These nanoparticles were collected on a filter and heat-treated at 673 K for 3 h. The experiments were conducted with a Ni/SiO_2 catalyst because the acidic surface of the silica does not adsorb CO_2[8] and, therefore, does not participate in the methanation mechanism. Supports with basic surface sites, in contrast, such as γ-Al_2O_3 or CeO_2, can participate in the mechanism and alter pathways.[16,17,65] CO_2 methanation experiments were performed in a catalyst testing unit with a differential fixed-bed setup at ambient pressure with a stoichiometric H_2/CO_2 mixture diluted in 75 % Ar at a weight-hourly-space velocity (WHSV) of $100\,\mathrm{L_N\,h^{-1}\,g^{-1}}$. A catalyst amount of 30 mg was used, which results in a length of the catalyst bed of 4 mm. The mixture was purified to remove oxygen and water contaminants. Ar was employed as an internal standard and to reduce thermal effects. A temperature-scanning experiment as described in Kreitz et al.[64] was used to investigate the methanation reaction over the entire temperature range up to 773 K. During the temperature scan, the temperature was linearly raised with a rate of $20\,\mathrm{K\,min^{-1}}$ (see Table S3 for a summary). The product mole fraction was analyzed with a high temporal resolution using a mass spectrometer. Based on the measured exit gas concentration and using Ar as an internal standard, the CO_2 conversion, CH_4 and CO selectivity, as well as CH_4 yield were calculated. Reaction rates, turnover frequencies, and activation energy were calculated for a conversion below 20 % assuming differential fixed-bed conditions. The catalyst was characterized with transmission electron microscopy, X-ray diffraction, N_2 physisorption, H_2 and CO_2 chemisorption, and temperature-programmed desorption. Further details on the catalyst production, catalyst characterization, the experimental setup, and evaluation can be found in Ref. 8 and 66 and are omitted here for brevity.

Microkinetic modeling

The experimental apparatus was modeled as a plug-flow reactor (PFR) using CANTERA,[67] which is an open-source suite of tools for problems involving chemical kinetics, thermodynamics, and transport processes. A PFR was chosen due to the differential fixed-bed conditions. The PFR was modeled as a series of 100 continuously-stirred tank reactors (CSTRs); the number of tanks was tested for convergence. A mean-field microkinetic model was assumed for the Ni(111) facet. All reactions were treated as reversible. Reaction kinetics were implemented in the forward direction, and the reverse rate constant was always calculated from the equilibrium constant, which ensures thermodynamic consistency. The temperature-scanning experiment was modeled by computing steady-state solutions at several temperature increments. This assumption is justified since no deviation between steady-state and transient results was observed in the experiments.[64] The parameters for the simulation are summarized in Table S3. As a simplification, no lateral interactions among the adsorbates were considered in the surface mechanism. The Python source code is available in the SI.

Parametric Uncertainty in Mechanism Generation

Global uncertainty analysis (GUA) was recently added to RMG as a post-processing tool exclusively for gas-phase mechanisms.[68] The effect of parametric uncertainty on the automatic mechanism generation process itself, in contrast, has not been previously investigated. A major component of the current work is to quantify how uncertainties in the model-generation parameters (*e.g.* heats of formation, activation energies) can influence the generated mechanism and the final model predictions. The heats of formation for the gas-phase species were taken from the Active Thermochemical Tables[69,70] and are known to within ± 0.001 eV; consequently, we assume these values to be "exact" and do not consider the impact of their uncertainty further.

For adsorbates, we assume that the binding energies (and thence heats of formation) are accurate to within ± 0.3 eV.[44,47,51] However, although the global uncertainty in adsorbate heats of formation might be ± 0.3 eV, the relative uncertainties between adsorbates is correlated, which is consistent with the LS concept.[31] As an approximate method for dealing with this correlation, we assume that all adsorbates that bind to the surface through the same element should be perturbed in the same direction. Rather than adjust the difference in adatom binding energies between Ni and Pt in Equation (1), we choose to adjust the adsorbate reference binding energy $\Delta E_{\mathrm{Pt}}^{\mathrm{AX}}$ by a fixed amount $\delta E_{\mathrm{Pt}}^{\mathrm{AX}}$ (see SI for explanation). Thus, the perturbed binding energies are given by:

$$\Delta E_{\mathrm{Ni}}^{\mathrm{AX}} = (\Delta E_{\mathrm{Pt}}^{\mathrm{AX}} + \delta E_{\mathrm{Pt}}^{\mathrm{AX}}) + \gamma \left(\Delta E_{\mathrm{Ni}}^{\mathrm{A}} - \Delta E_{\mathrm{Pt}}^{\mathrm{A}}\right) \tag{3}$$

Accordingly, since chemisorbed species are assumed to bind through either H, C, or O, we have three parameters – $\delta E_{\mathrm{Pt}}^{\mathrm{HX}}$, $\delta E_{\mathrm{Pt}}^{\mathrm{CX}}$, and $\delta E_{\mathrm{Pt}}^{\mathrm{OX}}$ – that adjust the heats of formation for the adsorbates. Additionally, physisorbed species (such as CH_4^*, CO_2^*, and H_2O^*) are not assumed to bind through a particular element and thus are not subject to the same LS relations; rather than treat them individually, we simply assume that well depths for all physisorbed species are correlated, which provides the fourth global parameter for adsorbate heats of formation, $\delta E_{\mathrm{Pt}}^{\mathrm{phys}}$. The range of possible values for $\delta E_{\mathrm{Pt}}^{\mathrm{HX}}$, $\delta E_{\mathrm{Pt}}^{\mathrm{CX}}$, and $\delta E_{\mathrm{Pt}}^{\mathrm{OX}}$ is $\pm 0.3\,\mathrm{eV}$; the range for $\delta E_{\mathrm{Pt}}^{\mathrm{phys}}$ is $\pm 0.2\,\mathrm{eV}$. Admittedly, this approach does not completely describe the true uncertainty (correlated and uncorrelated) in the heats of formation for adsorbates; nonetheless, it does capture how systematic errors in DFT-derived energies can be represented in model generation. A more detailed approach could provide different perturbations based upon bond order. Still, as will be demonstrated below, this simplified approach already reveals considerable information about the mechanistic response to parametric uncertainty.

Estimating the correlated uncertainty in the activation energy is an additional challenge. The uncertainties for activation energies should be larger than for binding energies. The BEP parameters E_a^0 and α are obtained from linear regression (typically to barrier heights obtained from DFT); accordingly, these parameters should be correlated.[71] However, information on the covariance matrix is seldom available in the literature. Therefore, we did not assume a correlation between α and E_a^0. Instead, we assume that both the intercept and the slope are uncertain and that the final activation energy is given by

$$E_{\mathrm{a}} = E_{\mathrm{a}}^{0} + \delta E_{\mathrm{a}}^{0} + (\alpha + \delta\alpha)\Delta H_{\mathrm{rxn}} \tag{4}$$

To be consistent with the uncertainty in the binding energies, the characteristic activation energy is perturbed $\delta E_{\mathrm{a}}^{0} \pm 0.3\,\mathrm{eV}$. The slope is perturbed $\delta\alpha \pm 0.15$; this perturbation is conservative compared to uncertainties reported in the literature.[62,72] Furthermore, the activation energy will be perturbed via changes to the binding energies of the reactants and products via Equation (3), which will change ΔH_{rxn}. Consequently, the total allowable change in the activation energy is larger than that of the binding energy and can vary significantly within a reaction family. As a simplifying assumption, the pre-exponential A was not adjusted. This restriction is rather crude, since pre-exponential factors can vary by an order of magnitude,[51] but for the temperature range of interest, the uncertainties in the activation energy will have a more significant impact on the overall kinetics. Lastly, we do not assume any correlation among the reaction families. Accordingly, the total number of perturbed parameters is 65: 4 parameters for adsorbate heats of formation, 1 parameter for the activation energy of CO_2^* dissociation, and 30 BEP relations (each with 2 parameters).

The next step is to evaluate how perturbations to these 65 parameters within their stated uncertainty bounds affect the size, complexity, and reactivity of the resulting mechanism. This task was accomplished in two stages. In the first stage, RMG was set to build exhaustive mechanisms by using smaller (tighter) convergence criteria (see Table S2). For this stage, a total of 500 distinct mechanisms were generated by employing a quasi-random sampling of the 65 parameters within the uncertainty range. Quasi-random numbers were generated with the low discrepancy Sobol sequence[73] using the SobolEngine from PyTorch.[74] As will be detailed below, these tighter criteria resulted in relatively large mechanisms, including the production of gas-phase products in the ppb range. This set of mechanisms are referred to as “coarse”.

In the second stage, the mechanism generation parameters were adjusted to build smaller mechanisms that focused more on the essential methanation kinetics; the convergence criteria were loosened, and a maximum number of carbon atoms of 3 was imposed (see Table S2 for complete values). For this stage, a new Sobol matrix of 65×5000 was generated, which resulted in a total of 5,000 unique mechanisms. This set of mechanisms are referred to as "fine". This dense sampling of the parameter space in the fine set will facilitate a global sensitivity analysis (GSA), described below.

Sensitivity Analysis

Global sensitivity analysis was performed to determine the parameters that contribute the most to the uncertainty of the output while considering the correlation among the input parameters.[75] The GSA was carried out with the UQTk package.[76,77] Polynomial chaos expansions (PCE) were used to build a surrogate model based on the 5,000 distinct mechanisms and the corresponding simulation results. PCEs allow analytical extraction of GSA indices via variance decomposition.[78] 4,500 model results were used to build the surrogate model with 3rd order polynomials, and 500 model results were used for the validation of the model. Total and joint sensitivity indices, measuring output variance contributions one or two parameter at a time, respectively.

The sensitivity indices quantify the contribution of the 65 parameters (LS and BEP parameters) to the observable (model) output variance. Therefore, the GSA in our study provides only information on the reaction families and descriptor species but not on on the importance of a single species or single reaction. A local sensitivity analysis was performed to quantify the important of individual species and reactions.[79] The mechanisms were evaluated with sensitivity analysis in a steady-state CSTR using the degree of rate control (DRC)[80–82] with respect to the methane formation rate, $r_{\mathrm{CH_4}}$, by

$$X_{\mathrm{RC}} = \frac{k_i}{r_{\mathrm{CH_4}}} \left(\frac{\partial r_{\mathrm{CH_4}}}{\partial k_i} \right) \tag{5}$$

where k_i is the forward rate constant of the elementary reaction i. In a brute-force (one-at-a-time) method, both forward and reverse rate constant were perturbed by 1 % for each reaction to maintain thermodynamic consistency. Additional DRC analysis was performed with respect to the stability (thermochemistry) of the adsorbates. The intermediates were stabilized by decreasing the standard state Gibbs free energy of formation $\Delta_{\mathrm{f}}G$ by 0.001 eV. The degree of thermodynamic rate control of the intermediates X_{TRC}[81,82] is given by

$$X_{\mathrm{TRC}} = \frac{1}{r_{\mathrm{CH_4}}} \left(\frac{\partial r_{\mathrm{CH_4}}}{\partial \left(\frac{-\Delta_{\mathrm{f}}G}{RT} \right)} \right) \tag{6}$$

The perturbations (1 % for rate constants, 0.001 eV for adsorbates) are assumed to be sufficiently small so that the local approximation is valid and that they are not correlated. The DRC for one mechanism has only limited meaning, given the broad range of parametric uncertainty assumed in the mechanism generation process. Accordingly, we performed the DRC analysis in Equation (5) and Equation (6) for all 5,000 mechanisms in the fine data set. As will be demonstrated below, this comprehensive DRC approach, which covers all possible combinations of parameters, identifies the global uncertainty of the DRC.[83]

Results and Discussion

Mechanism Generation for CO_2 Hydrogenation on Ni(111)

The initial set of 500 generated mechanisms with the coarse settings produced considerably different microkinetic mechanisms, with large variations in size (see Figure S13). The number of species and reactions in the core ranged from 21 to 64 species and 20 to 450 reactions;

the edge contained up to 360 more species and 1,053 different reactions. If we performed the mechanism generation with only one set of parameters, we would have missed possible pathways and intermediates. All generated mechanisms along with the evaluation is made publicly available in Ref. 84.

Mechanisms with many species/reactions were typically unreactive, which seems counter-intuitive at first, but it is a consequence of the flux-based mechanism-expansion procedure. The variability in mechanism size and reactivity is not a flaw of the method, nor is it unique to automated mechanism generation; instead, it is a natural consequence of the variability in model parameters within their stated uncertainties. Different density functionals that give systematically different (but otherwise correlated) energetics will result in different mechanisms; *e.g.* the microkinetic models proposed by Vogt et al.[10] and Lozano-Reis et al.[12] also show different number of species and reactions. The fact that most literature mechanisms contain fewer species/reactions has more to do with the computational cost of potential energy surface exploration than the intrinsic complexity of the kinetics. To reduce complexity, mechanism developers are forced to make assumptions that are not based on actual rates but rather experience, which adds bias.[29]

Figure 1a illustrates the full reaction network discovered from the coarse RMG settings. RMG discovered 64 unique species and 450 reactions in the core mechanism, with an additional 426 species and 1,205 reactions in the edge. The network contains multiple activation pathways for CO_2^*, including direct dissociation to CO^* and hydrogen-assisted dissociation, either via formate $HCOO^*$ or carboxyl $COOH^*$. RMG successfully predicted the methanation of CO_2 with various pathways for CH_4 formation. In addition to the expected products of CH_4, CO, and H_2O, RMG predicted numerous other gas-phase species such as ethene, ethane, propane, formaldehyde, methanol, ethanol, formic acid, and acetic acid. Additionally, the edge revealed that RMG considered pathways that lead to larger alkanes, alkenes, alcohols, and acids, with a maximum chain length of C_6.

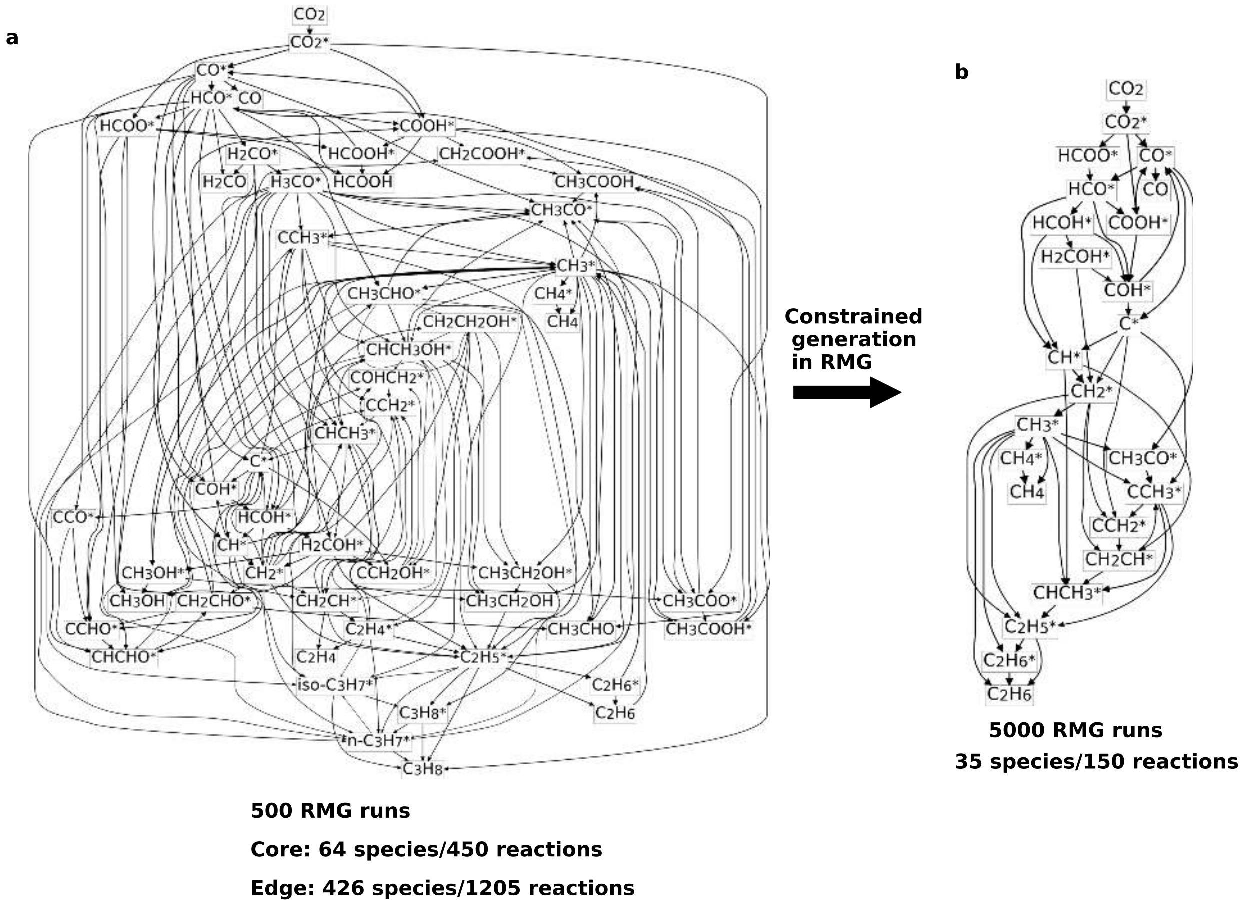
a
CO2
CO2*
CO*
HCO*
CO
HCOO*
COOH*
H2CO*
HCOOH*
CH2COOH*
H2CO
H3CO*
HCOOH
CH3COOH
CH3CO*
CCH3*
CH3*
CH3CHO*
CH4*
CH4
CH2CH2OH*
CHCH3OH*
COHCH2*
CCH2*
CHCH3*
C*
COH*
HCOH*
CCO*
CH*
H2COH*
CH3OH*
CH2*
CCH2OH*
CH3CH2OH*
CH3OH
CH2CHO*
CH2CH*
CH3CH2OH
CH3COO*
CCHO*
C2H4*
CH3CHO
CH3COOH*
CHCHO*
C2H4
C2H5*
iso-C3H7*
C2H6*
C3H8*
C2H6
n-C3H7*
C3H8
500 RMG runs
Core: 64 species/450 reactions
Edge: 426 species/1205 reactions
Constrained generation in RMG
b
CO2
CO2*
HCOO*
CO*
HCO*
CO
HCOH*
COOH*
H2COH*
COH*
C*
CH*
CH2*
CH3*
CH4*
CH3CO*
CH4
CCH3*
CCH2*
CH2CH*
CHCH3*
C2H5*
C2H6*
C2H6
5000 RMG runs
35 species/150 reactions

Figure 1: a) Full reaction network of the core mechanism for the hydrogenation of CO_2 on Ni(111) obtained from coarse generation settings. b) Constrained reaction network from the fine mechanism generation process.

Although RMG successfully found multiple gas-phase products, that does not imply that these species are produced in meaningful quantities. Simulations with all 500 mechanisms demonstrated that only CH_4, CO, and H_2O are produced in significant amounts (a few percent) (see Figure S14), which is expected since Ni is a selective methanation[7,9] or RWGS catalyst[12,19,20] depending on the conditions. The gas-phase product with the highest yield from the side products is ethane, with concentrations of a few ppm; the other gas-phase species had concentrations of a few ppb. Ethane and propane were also observed experimentally over Ni/Al_2O_3[85,86] and Ni/SiO_2 catalysts,[10] which suggests that these pathways do indeed exist.

Although it would be feasible to perform sensitivity analyses for these larger mechanisms, it is neither practical nor useful. Additional gas-phase products, and the numerous surface intermediates that are necessary for their production, do not influence the main CH_4 formation pathways. For the fine sampling (5,000 RMG runs), the maximum number of carbon atoms was restricted to 3 and the tolerance parameters were loosened to simplify the more detailed mechanism analysis. The reaction network that results from the fine generation process is illustrated in Figure 1b.

The mechanism for CO_2^* methanation is grouped into three main pathways: the formate path (via $HCOO^*$), the carboxyl path (via $COOH^*$), and the redox/carbide pathway with a direct dissociation of CO_2^* to CO^*.[10,12] In the formate path, CO_2^* is activated by H^* at the carbon atom. $HCOO^*$ then dissociates to formyl (HCO^*), which is further hydrogenated to hydroxymethylene ($HCOH^*$) and then hydroxymethyl (H_2COH^*). The C−O bond in hydroxymethyl is then cleaved, forming hydroxyl (OH^*) and methylene (CH_2^*). In the carbonyl pathway, CO_2^* activation occurs at the oxygen atom; the resulting $COOH^*$ can then cleave either the C−O or C=O bond to yield carbon monoxide (CO^*) or hydroxymethylidyne (COH^*), respectively. Direct CO_2^* dissociation occurs in the redox pathway forming CO^*, which can desorb directly or undergo further bond fission to form surface carbon that is subsequently hydrogenated to CH_4. These three pathways are not separate mechanisms; rather, they are coupled pathways entangled by various abstraction and dissociation reactions.[10,12] Importantly, as depicted in Figure 1b, RMG found all three major CO_2^* activation routes, as well as the numerous cross-coupling reactions. The constrained mechanisms still contains the production of ethane via various C−C coupling reactions like $C{-}CH_x$, $CH_x{-}CH_y$, or $CH_y{-}CO$.

The combined reaction network discovered by RMG for all 5,000 runs contains 35 species and a total of 150 reactions. Of these reactions, 9 are adsorption/desorption, 36 are dissociation, and 105 are abstraction (see Table S9). The high number of abstraction reactions is in sharp contrast to most of the literature studies, where only dissociation reactions are considered.[10,14,15] Some abstraction reactions were considered by Lozano-Reis et al.,[12] but usually these types of reactions are overlooked due to the combinatorial growth of possible reactions to consider.[29,30] The abstraction reactions are not limited to the oxidative dehydrogenation reactions of R−H by O^* or OH^*. Larger moieties can be abstracted further down the chain, which creates a whole new set of reactions that are currently not considered in the literature. The presence of these abstraction reactions nicely illustrates the full potential of automated mechanism generation.

The C_1 species discovered are consistent with prior literature mechanisms,[10,12,14,15] with the most sophisticated study by Lozano-Reis et al.[12] It is worth emphasizing that none of these species were included in the input, and thus RMG did not "know" to look for them. Additionally, several new abstraction reactions were predicted by RMG, which have not previously been considered for methanation. Furthermore, none of the other studies includes the formation of C_2 species, even though it is experimentally observed.[10,85,86] A predictive microkinetic mechanism should capture all the important pathways that lead to experimentally observable products, even if C−C coupling does not represent a major competing pathway for methanation under the present conditions.

Microkinetic Modeling

Figure 2 shows the experimentally recorded concentration profiles for all species measured during the temperature-scanning experiment on a dry basis (except Ar). The carbon mass balance is always closed within ±2 %. With the current setup, it is not possible to accurately measure the H_2O concentration due to partial condensation in the transfer lines. The experiments show a starting temperature for the CH_4 formation around 500 K, followed by a pronounced CO peak with a maximum at 550 K. A maximum CH_4 formation rate is observed at a temperature of 650 K, with a CH_4 selectivity of 97 %. The CH_4 concentration decreases at higher temperatures, whereas the CO concentration increases according

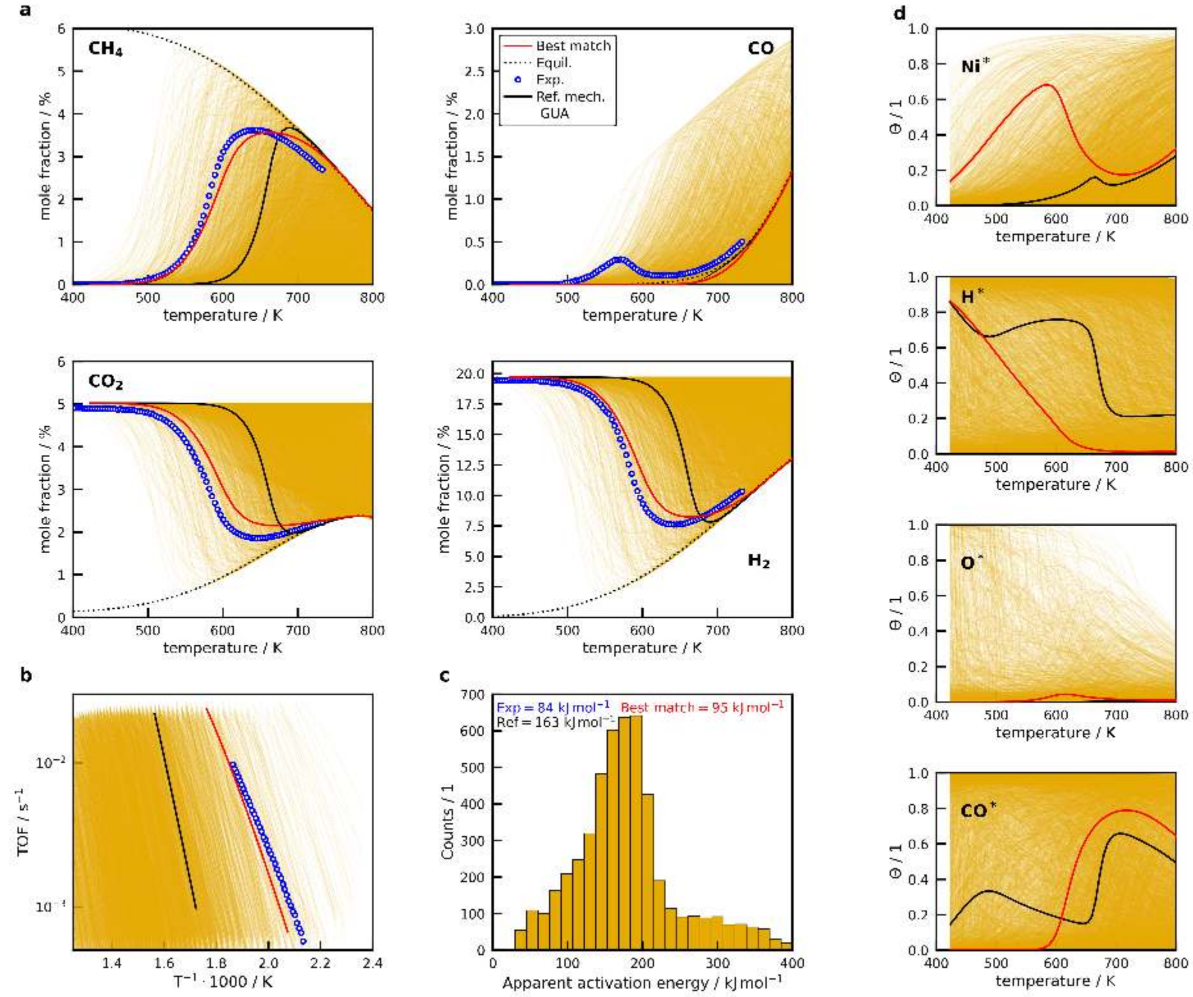

Figure 2: (a) Comparison of measured (open blue circle) and simulated (lines) mole fractions (on dry basis) for the temperature-scanning experiment using the microkinetic models generated by RMG. The dotted black line corresponds to the thermodynamic equilibrium and the solid black line to the generated reference mechanism. The colored area consists of all generated mechanisms. (b) Comparison of the measured and predicted TOFs. (c). Histogram of apparent activation energies calculated from the slope of the TOFs. (d) Simulation results for the four species with highest coverage.

to thermodynamic equilibrium that is reached in the experiment at temperatures beyond 700 K. An activation energy of 84 kJ mol^{-1} was determined, which is comparable to other Ni/SiO$_2$ catalysts.[10,64,87,88] Results from the microkinetic model generated by RMG with the reference settings shows a significantly lower activity at lower temperatures. CH$_4$ formation starts at 600 K and reaches the maximum rate at 700 K. The production of CO starts at a temperature of 650 K and directly reaches the equilibrium concentration.

Also included in Figure 2 are the reactor simulations using the 5,000 different mechanisms. All generated mechanisms adhere to the thermodynamic constraints, which was confirmed according to literature guidelines[89,90] (see SI). The predicted profiles range from almost no CH_4 formation even at high temperatures to an increased activity at low temperatures, with maximums of $5\,\%$ at $600\,K$. This broad range in reactivity is a consequence of the approximate $\pm\,0.3\,eV$ uncertainty in energies obtained from electronic structure calculations. In other words, for some combination of parameters, the Ni(111) facet is inactive for methanation but only produces CO via the RWGS reaction, and thus other facets should be considered.[10,12] For other parameter combinations, in contrast, the Ni(111) surface exhibits quite a high methanation activity, also in agreement with the literature,[10,15] and could, therefore, be the active site. Accordingly, it is difficult to establish the importance of the Ni(111) facet for CO_2 methanation with confidence, given the current parametric uncertainty of DFT data.

Figure 2b presents the turnover frequency (TOF) for the system, which was calculated from the average CH_4 formation rate and the amount of exposed Ni surface atoms in the PFR. Figure 2c presents a histogram of the corresponding apparent activation energy. Most of the mechanisms exhibited very low activity as can be seen by the dense cluster of lines at higher temperatures in the TOF plot and the broad range of comparatively high activation energies. This distribution in activity is consistent with the Sabatier principle; high activity is only obtained when key intermediates are bound to the catalyst neither too strongly nor too weakly.

Figure 2d summarizes the surface site fractions for the vacant site (Ni^*) and the three adsorbates with the highest coverages (H^*, O^*, CO^*). Profiles for other adsorbates, as well as for CO_2 conversion, CH_4 selectivity, and CH_4 yield are provided in the SI. Depending upon the particular combination of parameters, the surface can be entirely vacant, completely blocked by either H^* or CO^*, or in a few instances, covered by O^*. This range in coverage suggests that it is challenging to make *a priori* assumptions regarding the most-abundant surface intermediates (MASI) with any confidence. The predicted coverages of the reference model are in contrast to the results reported by Vogt et al.,[10] who report a Ni(111) surface that was completely saturated with CO^*, but they did not include the possibility of CO^* desorption. In contrast, Lozano-Reis et al.[12] obtained a nearly vacant Ni(111) surface with just around 10 % H^* coverage. Heine et al.[13] observed CO^* on the Ni(111) surface at elevated temperatures during CO_2 methanation, which agrees with the model predictions.

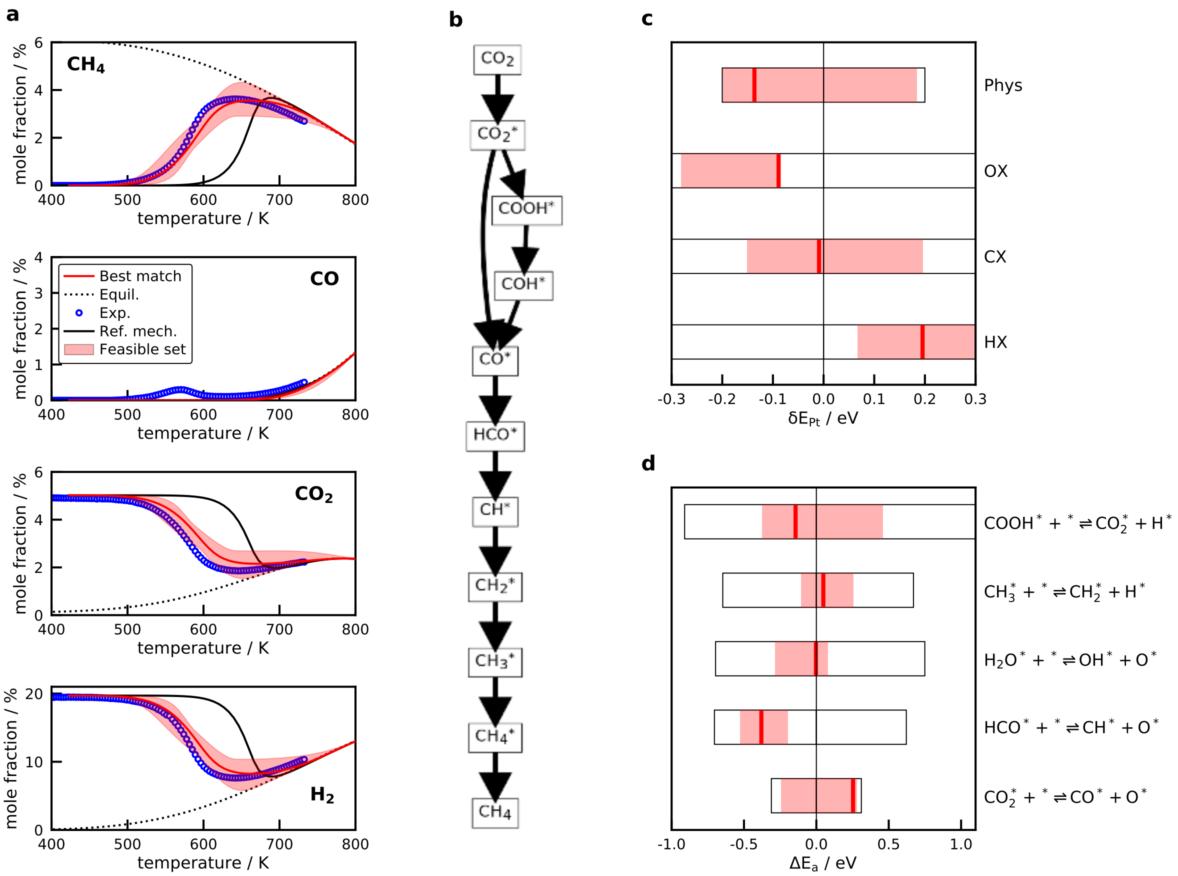

Figure 3: a) Comparison of the experiments with the mechanisms with the closest agreement to the data from the global uncertainty analysis. The solid black line is the base-case mechanism; the solid red line is the mechanism with the lowest MAPE, and the shaded pink region contains the mechanisms that are within +30 % of the lowest MAPE (the “feasible sets”). b) Reaction network of the mechanism with the lowest MAPE compared to the experimental data. Only the intermediates and pathways that contribute significantly to the CH_4 formation rate are displayed. c) Values for the LS descriptor species and d) the kinetic parameters for the most important reactions. The black box shows the possible range of values and the pink area the values from the feasible sets.

From the computed profiles in Figure 2, it is possible to identify the subset of mechanisms in closest agreement with the experimental data. The mechanism that had the lowest overall mean-absolute percentage error (MAPE) for the predictions of all four species against the experimental data is shown as a red line in Figure 2. Additionally, there are multiple combinations of parameters that are within 30 % of the lowest MAPE. This ensemble of feasible mechanisms, along with the closest match, are illustrated by the shaded pink region in Figure 3a. It should be emphasized that the red line in Figure 2 and 3, although in quantitative agreement with the measured data, is not in any way a fit or optimization. All the parameters were selected within their stated uncertainty ranges consistently with their correlated uncertainties. The agreement with measured concentrations certainly could be improved by optimizing the pre-exponential factors, optimizing the binding energies and activation energies (within a narrower range), and accounting for coverage dependence, but such an attempt at optimization is beyond the scope of the present work.

The essential pathways for the methanation of CO_2 on Ni(111) are illustrated in Figure 3b. At a temperature of 573 K, 75 % of CO^* is produced via the direct dissociation of CO_2^*, and the remaining 25 % comes from various reactions in the carboxyl path, which contradicts conclusion from Vogt et al.,[10] who argued that this path does not contribute to CH_4 formation. The only significant source of CH^* (and thus ultimately CH_4^*) is from the dissociation of HCO^*, $HCO^* + CH^* \longrightarrow O^*$. According to the DRC analyses for all 5,000 mechanisms, there is no combination of parameters in which the formate path, $CO_2^* \longrightarrow HCOO^* \longrightarrow HCO^*$, is a significant source of HCO^* (see SI for details). Instead, the overwhelming majority of HCO^* is produced via hydrogenation of CO^*, $CO^* + H^* \longrightarrow HCO^*$, where CO^* is produced via the redox and carboxyl path. This result is in agreement with Heine et al.,[13] who did not observe $HCOO^*$ during CO_2 methanation on Ni(111) in operando XPS studies. Although $HCOO^*$ has been observed in some spectroscopic studies[9,10,91,92] during CO_2 hydrogenation on Ni, our findings support the conclusion that $HCOO^*$ is a spectator species.[19,91,92]

Figure 3c presents the best match and feasible set for the four parameters that govern the correlated binding energies. The results suggest that all mechanisms in the feasible set require an increase to the heat of formation for H^* (*i.e.* destabilize), and a decrease to the heat of formation of species that bind through oxygen. Variability in the binding energy of adsorbates that bind through carbon, in contrast, is not as important. Figure 3d presents similar results for the top five reactions (see Sensitivity Analysis); the most significant deviation from the base case is for HCO^* dissociation, where the feasible set is more tightly clustered around a reduction in the activation energy of 0.4 eV.

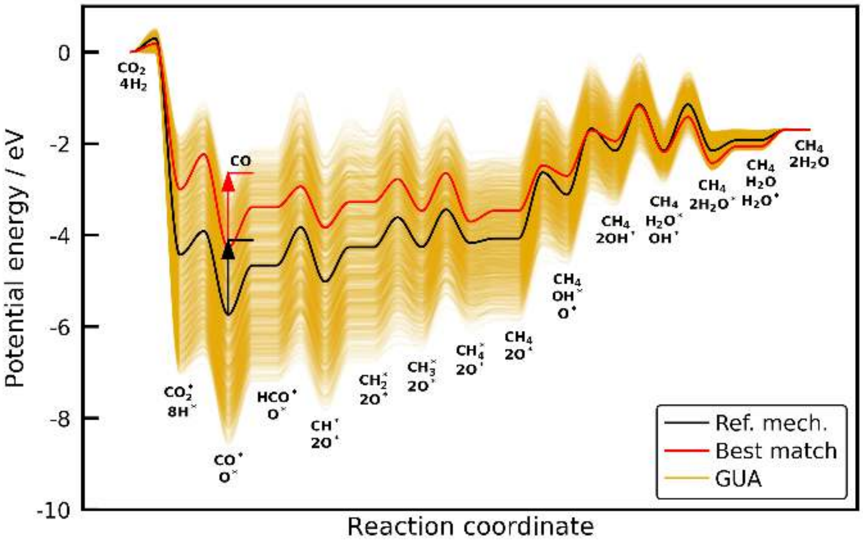

Figure 4: Potential energy diagram for the most dominant CH_4 formation pathway. The balancing H^* atoms are omitted for clarity after the adsorption step. Only a reduced number of 1000 mechanisms is displayed for clarity.

A subset of the potential energy diagram that highlights the main pathway is presented in Figure 4. The individual yellow lines represent different possible mechanisms. The large spread in possible values in the initial portion of the potential energy diagram is due primarily to the fact that there are 8 H^*. Adsorbates that bind through carbon (*i.e.* C^*, CO^*, HCO^*) represent the various minima for the first half of the diagram. The difference between the base case (solid black line) and the best match (solid red line), combined with the results from Figure 3d, indicates that the majority of the change from the black line to the red line comes from the weakening of the H^* binding energy by 0.2 eV; the binding energies for adsorbates that bind through carbon are not changed significantly. Adsorbates that bind through oxygen (*i.e.* O^*, OH^*) represent the second half of the diagram. Here we see that a decrease in the heats of formation (stabilizing) of 0.1 eV of species that bind through oxygen is needed to improve the agreement. The parameterized mechanism of this reduced network is provided in Table S10 and the complete mechanism in Table S11.

The species lowest in potential energy are H^* and CO^* and, therefore, most likely to be the MASIs on the Ni(111) surface, which also agrees with the simulation results. High activation barriers are obtained for HCO^* formation and dissociation, as well as the hydrogenation of O^* and OH^*. CO does not desorb in the best cases because the desorption barrier is significantly higher than the hydrogenation to HCO^*. There are several routes for the activation of CO_2^* in the carboxyl pathway with comparable barriers (see Table S10 and Figure S19 for the free energy surface); either via reaction with H^*, or CO_2^* can abstract a H atom from OH^* or H_2O^*. After the creation of $COOH^*$, there are two possible routes with comparable free energy barriers for its decomposition, with the cleavage of C=O or C−OH. The formation of CO from COH requires an additional step, and the oxidative dehydrogenation of COH^* provides a significantly lower barrier than the direct dissociation, in agreement with results from the activation of CO on Co in the Fischer-Tropsch synthesis.[27] BEP relations providing barriers for bimolecular reactions are coupled to the thermochemistry of multiple species, so the uncertainty range of the barrier can be large. Consequently, the activity of these pathways, which are all relatively close in free energy, can contribute to various extents to the CH_4 formation in the parametric uncertainty range. Figure 4 and Figure S19 actually show that it is currently difficult to predict a certain path within the given accuracy of the present DFT functionals.[47,52,53]

Although the microkinetic model can accurately predict the measured CO_2 conversion and CH_4 yield, it is currently not able to accurately predict the correct selectivities towards

CH_4 and CO at low temperatures (see Figure 2a and Figure S16). Some simulations show a CO desorption peak at low temperatures, but this can only occur if the binding energy of CO is lowered, so that CO can partially desorb from the catalyst surface before the activation barrier of the step consuming the CO^* is overcome. A likely explanation for the discrepancy in the selectivity is coverage dependence.[93] As mentioned above, no coverage effects were considered in the present study. However, adsorbates like CO^* or O^* show repulsive interactions, which destabilize their binding energies.[20,94] In general, including coverage effects will affect the binding strength of species and transition states and can significantly alter the potential energy surface.[46,51] Thus, we suspect that the inability of our model to describe the CO desorption peak is a consequence of neglecting coverage effects, not due to missing kinetic pathways. The inclusion of coverage effects directly in the mechanism generation procedure is the aim of future studies.

Analysis

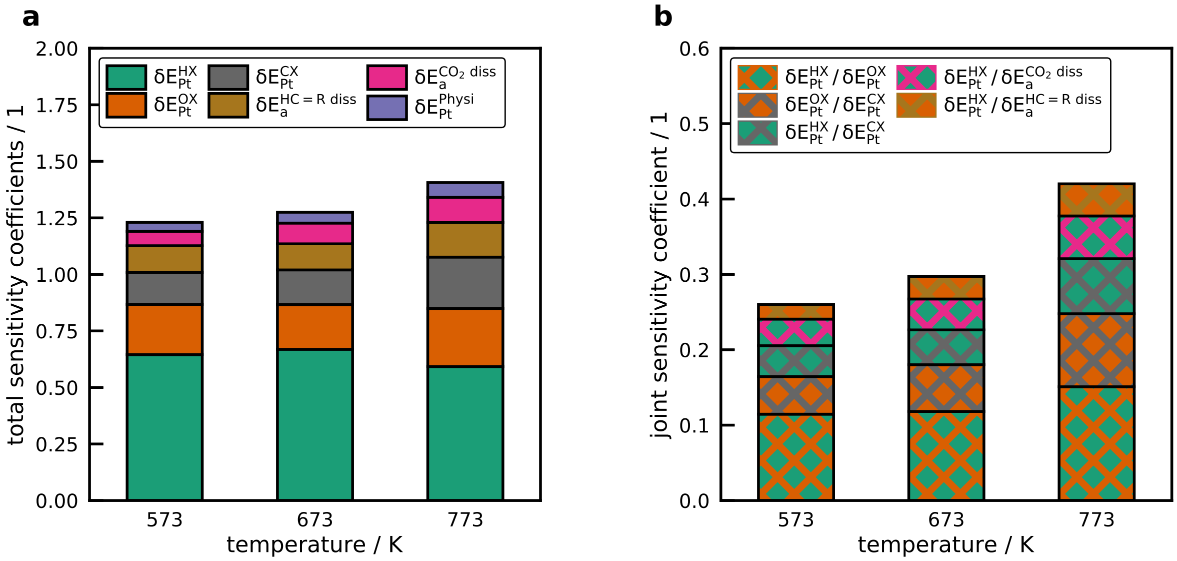

Figure 5: a) Total sensitivity coefficients for the 6 most influential input parameters on the uncertainty of the CH_4 concentration at different temperatures. b) The joint sensitivity coefficients with the highest values. The hash combines the pair of colors from the total sensitivity coefficients.

In a microkinetic model, not all species and reactions are equally important; typically, the variability of the output is determined by just a few species and reactions. The total sensitivity coefficients for the CH_4 concentration, determined from the polynomial chaos expansion, are displayed in Figure 5a. Of the 65 parameters that were varied in the global uncertainty analysis, the parameter with the largest sensitivity index is for $\delta E_{\mathrm{Pt}}^{\mathrm{HX}}$, which corresponds to the heat of formation of H^*. This result is unsurprising, given that hydrogenation reactions are critical in methanation and that the heat of formation of H^* affects activation barriers via BEP relation and reverse rates via the equilibrium constant. The next most important parameters are $\delta E_{\mathrm{Pt}}^{\mathrm{CX}}$ and $\delta E_{\mathrm{Pt}}^{\mathrm{OX}}$ for the heats of formation of adsorbates that bind through oxygen and carbon, respectively. The larger influence of thermochemistry than kinetics was observed in other studies as well.[45]

The fourth most important parameter is the reference activation energy for the reaction family for the dissociation of HC=R double bonds. This family provides kinetics for the dissociation of the C=O bond in HCO^*, which many studies consider to be the RDS.[10,15] Moreover, this reaction is the most important pathway for CH^* formation observed in the mechanisms with best agreement to the experiments (see Figure 3b and Figure 4). The next most sensitive reaction is CO_2^* dissociation, which is also thought to be rate controlling.[12]

In a complex microkinetic model, there will be higher-order interactions among the parameters, which are further amplified by the coupling of the thermochemistry with the activation barriers in the BEP relations. These higher-order interactions are captured by the joint sensitivity indices from the PCE method and displayed in Figure 5b. The highest joint sensitivities are caused by H^* in combination with O^*, C^*, CO_2^* dissociation, and the HC=R dissociation family.

Figure 6 summarizes the results of the degree of rate control analysis. The black boxes in Figure 6a-b represent the range of possible DRC values at 573 K for reactions and species, respectively, that were obtained for the entire set of 5,000 mechanisms. Also included inside each box is the DRC value for the best match (vertical red line) and the ensemble of

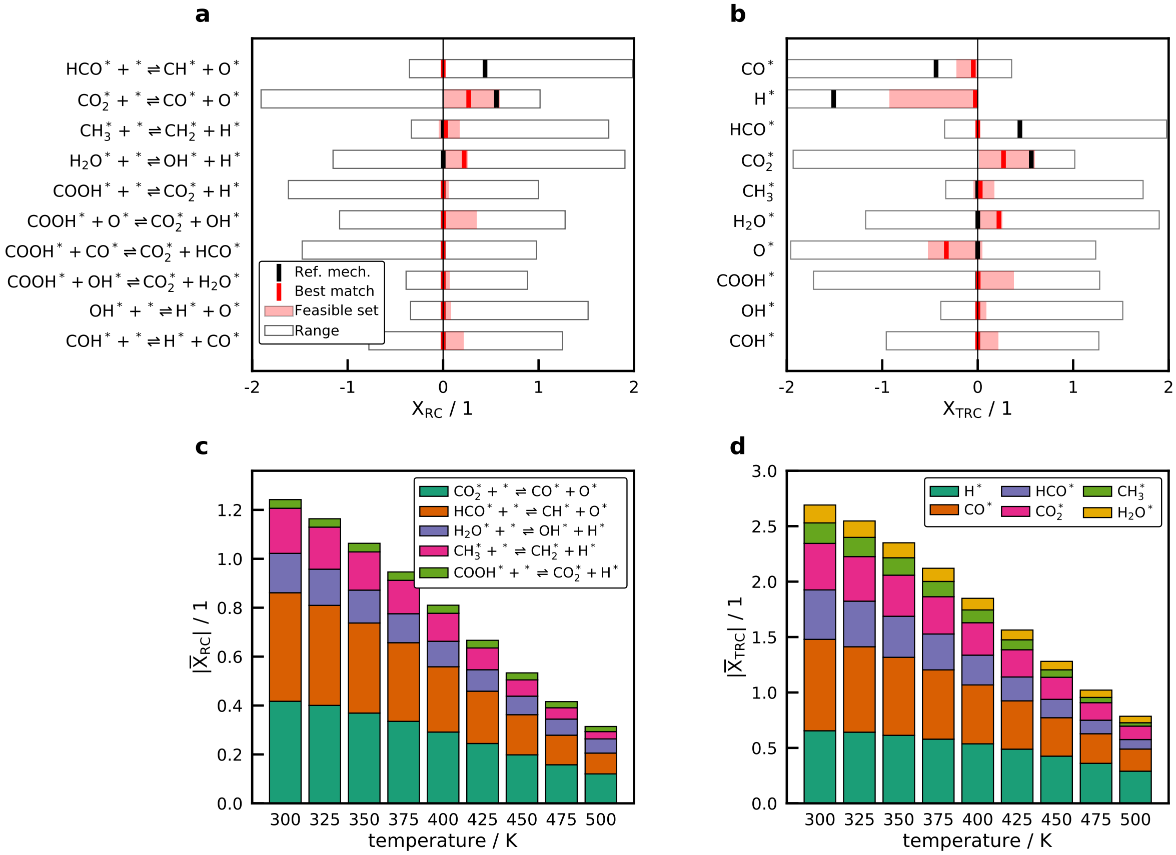

Figure 6: DRC for (a) reactions and (b) adsorbates at 573 K. Only the 10 most important reactions/species are presented, with the reactions/species with the highest absolute average DRC at the top. The black box represents the range of the DRC values for all possible mechanisms; the black line is the base set; the red line and pink shaded region are the best mechanism and feasible set, respectively. Averaged absolute c) DRC and d) thermodynamic DRC at different temperatures.

feasible mechanisms (shaded pink region). According to the DRC analysis, the most important reactions are the dissociation of CO_2^* and the dissociation of the C=O bond in HCO^*, in agreement with the results from the GSA, the network from the best match, and the literature.[10,12,15]

The results in Figure 6a-b nicely highlight the implicit assumptions in the DRC approach and associated challenges that it entails. For the overwhelming majority of parameter combinations, the dissociation of HCO^* has a positive DRC, implying that increasing the rate constant will increase the rate of CH_4 production. For the feasible set, however, it is zero.

The dissociation of CO_2^*, in contrast, has a X_{RC} that ranges from -2 to value near 1. Additionally, abstraction reactions that convert CO_2^* to $COOH^*$, which are frequently neglected, are rate controlling for some parameter combinations. Equally important, the actual values of X_{RC} for a given reaction can vary considerably. Vogt et al.[10] and Zhou et al.[15] report that the dissociation of HCO^* is the RDS on Ni(111), whereas Lozano-Reis et al.[12] state that the dissociation of CO_2^* is the RDS. The present results suggest that the choice of RDS is, in fact, highly dependent on the microkinetic parameters (and thus the method through which they were obtained). Indeed, both of these reactions and many others can be rate-controlling, depending upon small perturbations of parameters within a narrow uncertainty range. For the best match mechanism, CO_2^* dissociation has the largest X_{RC}. The DRC analysis shows that from all 150 elementary reactions, only a handful have high DRCs over the entire uncertainty range and the rest are never rate-controlling (see Figure S22).

From the thermodynamic DRC, we obtain that the most important species are CO^*, H^*, HCO^*, and CO_2^*, which can also be anticipated based on X_{RC}. Also, according to Stegelmann et al.[81] and Wolcott et al.[95] X_{TRC} is correlated to the coverage, and CO^* and H^* are the MASIs. Both CO^* and H^* have predominantly negative X_{TRC}, and thus increasing the stability of these two species on Ni(111) will inhibit the CH_4 formation rate. HCO^* exhibits the opposite behavior; increasing the stability of this species will increase the CH_4 formation rate. CO_2^* shows a complex behavior of the sensitivity coefficients. Stabilizing CO_2^* can lead to an increase in the CH_4 formation rate in some cases, whereas it is inhibiting in others. For the other species in the mechanism, the results are more complicated. On average, their contribution to the production rate is small, but each one can have a controlling effect for some parameter combinations. Perhaps the most surprising result from Figure 6a-b is that, for the mechanisms that are in closest agreement with the experimental data, most reactions/species have DRC values close to zero. An additional observation from this analysis is that some species can have a high X_{TRC} although they have no significant coverage over the entire uncertainty range (see Figure S15), which calls into question the correlation between

X_{TRC} and coverage in complex microkinetic models.

In the absence of experimental data, it would not be possible to determine *a priori* which mechanism will provide the closest description of reality – let alone speculate as to the reaction/species with the highest DRC. Accordingly, averaging over the DRC of all mechanisms is a compelling way to predict how the mechanism is likely to respond in the absence of other information. Additionally, it prioritizes which rate constants or thermochemistry should be refined. Figure 6c-d plots the average of the absolute value of the DRC at different temperatures for reactions and species, respectively. These figures demonstrate that 4 reactions and 6 species have a high DRC over the entire temperature range. Of these results, the CO_2^* and HCO^* dissociation, together with heats of formation for the H^* and CO^*, are most important, which is consistent with the GSA and the literature.[10,12,15] Thus, every effort should be made to refine the kinetic and thermodynamic parameters for these reactions and species as accurately as possible. However, comparing Figure 6c-d with Figure 6a-b highlights how varied the DRC results can be, depending upon the structure of the underlying mechanism.

A key finding in Figure 6a-b that critical reactions (CO_2^* and HCO^* dissociation) and species (H^* and CO^*), can exhibit enormous variability in DRC, depending upon the model parameters. Figure 7a-c illustrates this variability in X_{TRC} for H^* and X_{RC} for the CO_2^* and HCO^* dissociation over the variation in the uncertainty range. If we focus on the DRC for CO_2^* dissociation (7b), we observe two broad clusters. For negative values of ΔE_{a}, the X_{RC} tend to be clustered around 0.0 (because a low barrier leads to a higher rate), and for positive values of ΔE_{a}, the X_{RC} tend to be clustered around 1.0. However, in both cases, there is considerable scatter. Moreover, the feasible set (represented by the red squares) spans the entire horizontal range, with no clearly discernible trend. The results for HCO^* dissociation (7c), in contrast, show more structure. The results from the feasible set are all tightly clustered around $-0.6 < \Delta E_{\mathrm{a}} < -0.2$, which result in $X_{\mathrm{RC}} = 0$. When the activation energy for this reaction is increased, the reaction shifts from $X_{\mathrm{RC}} \approx 0$ to $X_{\mathrm{RC}} \approx 1$ and it becomes

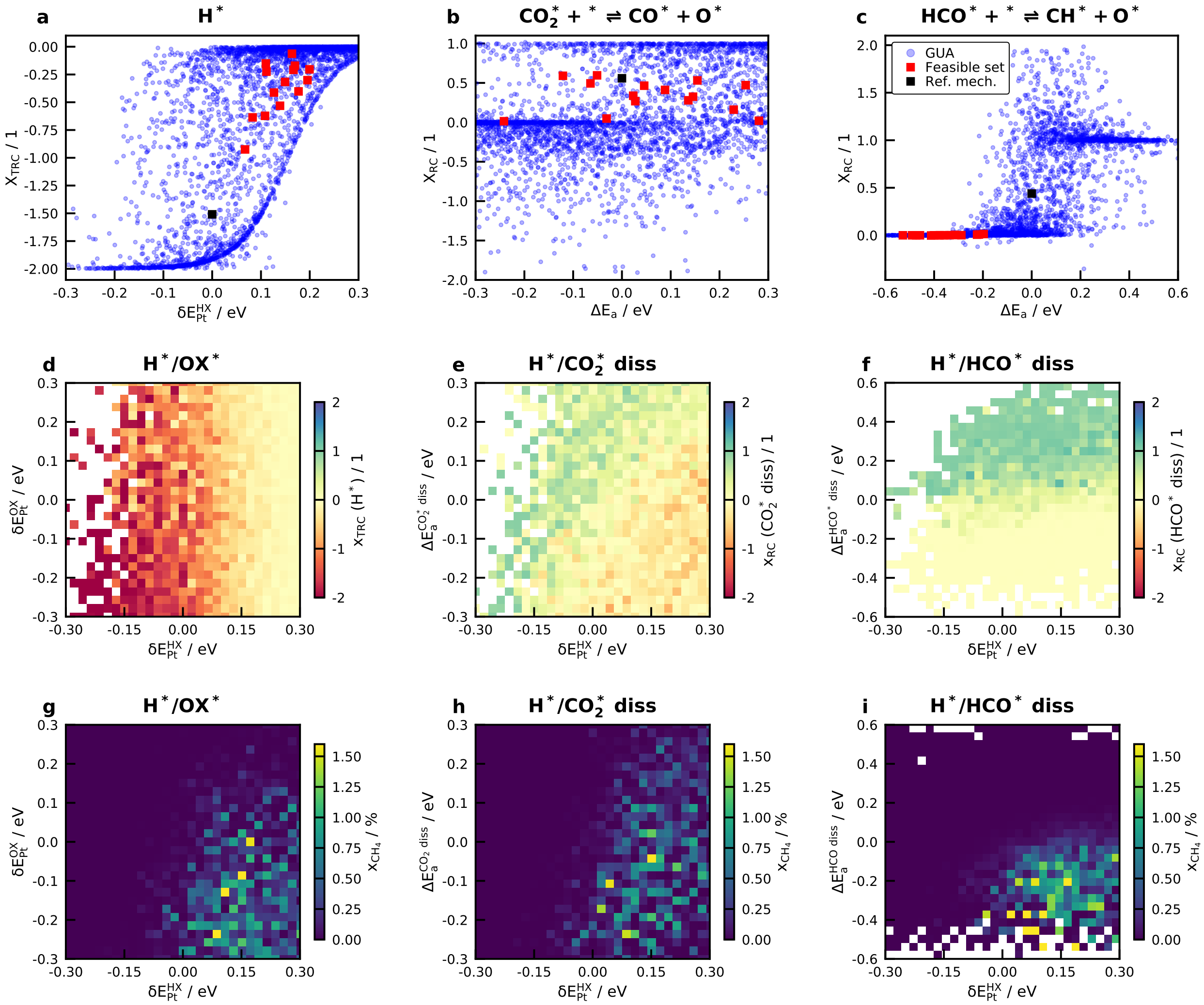

Figure 7: Scatter plots for a) X_{TRC} of H^* versus change binding energy, b) X_{RC} of CO_2^* dissociation, and c) X_{RC} of HCO^* dissociation versus change in activation energy. Red squares are the values for mechanisms in the feasible set, and the black square is the reference mechanism. d) Heatmap for X_{TRC} of H^* over $\delta E_{\mathrm{Pt}}^{\mathrm{HX}}$ and $\delta E_{\mathrm{Pt}}^{\mathrm{OX}}$. Heatmaps for the DRC for the e) CO_2^* and f) HCO^* dissociation as a function of their change in activation energy and $\delta E_{\mathrm{Pt}}^{\mathrm{HX}}$. Heatmaps for CH_4 mole fraction as a function of $\delta E_{\mathrm{Pt}}^{\mathrm{HX}}$ and g) $\delta E_{\mathrm{Pt}}^{\mathrm{OX}}$, h) activation energy of CO_2^* dissociation, i) activation energy of HCO^* dissociation. The data are sorted into a 30×30 grid and all sensitivity coefficients or CH_4 mole fractions are averaged in these bins. All results are for a temperature of 573 K.

the RDS. Another clear trend is obtained for the thermodynamic DRC for H^* (Figure 7a); as H^* is stabilized on the surface, it has an increasingly inhibiting effect.

By combining these results with the joint sensitivity coefficients from Figure 5b, we can begin to see what other parameters contribute the most to the scatter in Figure 7a-c. Specifically, for both reactions, the parameter with the highest joint sensitivity coefficient is $\delta E_{\mathrm{Pt}}^{\mathrm{HX}}$ (and therefore the heat of formation for H^*). Variation in X_{TRC} for H^* in Figure 7d is mostly vertical; it goes from 0 to -2 as $\delta E_{\mathrm{Pt}}^{\mathrm{HX}}$ is decreased (and thus H^* is made more stable), but $\delta E_{\mathrm{Pt}}^{\mathrm{OX}}$ has very little effect. The surface is covered in H^* under these conditions (see Figure S30), which agrees with observations that X_{TRC} is linked directly to surface coverage.[81,95] Figure 7e,f present heatmaps for X_{RC} of CO_2^* and HCO^* dissociation, respectively. In Figure 7e, the values of $X_{\mathrm{RC}} \approx 1$ are generally clustered between $-0.3 < \delta E_{\mathrm{Pt}}^{\mathrm{HX}} < -0.1$, suggesting that CO_2^* dissociation is only rate controlling when H^* is stabilized on the surface. At these conditions the surface is covered in H^* and lacks CO^*, which is why the production of CO^* via CO_2^* dissociation is rate-controlling. However, the HCO^* dissociation is rate controlling over the entire uncertainty range of $\delta E_{\mathrm{Pt}}^{\mathrm{HX}}$ (Figure 7f). Figure 7d-f clearly indicate that the DRC can change from insensitive to rate controlling within the range of a few meV.

Figure 7g-i present heatmaps for CH_4 mole fraction as a function of $\delta E_{\mathrm{Pt}}^{\mathrm{OX}}$ as well as the barrier for CO_2^* and HCO^* dissociation in combination with $\delta E_{\mathrm{Pt}}^{\mathrm{HX}}$. Other key parameters are reported in the SI. In Figure 7h for CO_2^* dissociation, we can see a vertical area where CH_4 formation is feasible, which is when H^* is destabilized, without a clear dependence on the activation barrier. Figure 7i shows that CH_4 is only produced when H^* is destabilized and the barrier for HCO^* dissociation decreased. When the activation barrier for the HCO^* dissociation is increased, no further conversion pathways for CO^* are available, and the surface will be poisoned by CO^*, thereby inhibiting H^* adsorption. Since the activation barrier is determined from the BEP, these points coincide with the pattern for the O^*/H^* dependence (see Figure 7g). A decrease in O^* heat of formation lowers the heat of reaction and thus the activation barrier. Looking at the scatter plot (Figure 7c), we can now state that HCO^* dissociation is never rate-controlling when CH_4 is formed, which is why it has also a small DRC for the best cases, and other reactions are rate controlling instead, *e.g* CO_2^* dissociation. Collectively, however, these results all indicate that the HCO^* dissociation in combination with H^* and O^* binding strength are the true factors that control the methanation activity of the Ni(111) facet. This can also be seen in Figure 3c-d, where these three parameters show a clear grouping of values for the feasible set of parameters that agree well with the experimental data. These results highlight a severe limitation of the DRC analysis given the large uncertainty of DFT parameters. The factors that control the methanation activity locally (DRC) are not the same as the global properties that truly determine the methanation activity. Only when H^* is destabilized can other important intermediates (*e.g.* CO^*, O^*) cover the surface and the destabilization decreases several activation barriers. A high CO^* and O^* coverage favor CH_4 production; the H^* surface site fraction for the best cases are actually rather small (see Figure S18). Furthermore, we have seen that all steps with high DRC values are part of the reduced methanation mechanism. Based on our insights gained from the global sensitivity analysis and the global uncertainty of the DRC, we can further hypothesize that the reduced microkinetic model (see Figure 3b and Table S10) determines the methanation activity over the entire uncertainty range, making it the most likely methanation mechanism for the Ni(111) facet.

Finally, we wish to emphasize that the purpose of this analysis is not to provide a definitive mechanism for CO_2 methanation on Ni. In fact, it is difficult to state conclusively whether or not Ni(111) is the active facet. Although the microkinetic mechanism agrees with the experimental data with remarkable predictive power, self-consistent sets of parameters can yield virtually every conceivable outcome within this confined uncertainty space of $\pm$ 0.3 eV. This is neither a flaw in this study, the applied methods, nor automated mechanism generation in general. Since all assumptions on the uncertainty in this study represent only the accuracy of present DFT functionals, it indicates that it is not possible for a pure DFT study to conclusively determine the activity of the Ni(111) facet either. Moreover, this result is not unique to methanation; a large variation in activity was also observed by Sutton et al.[45] for ethanol steam reforming. However, with the automated mechanism generation, we were able to derive a complete mechanism including all the possible chemistry as well as unravel the reactions and parameters that control the activity over the entire uncertainty range (see

Figures 3, 6 and 7), which cannot be done with typical DFT studies.

Ultimately, it will be necessary to repeat this procedure for all four Ni facets independently and combine them in a multifacet model, as has been done in previous work by some of the authors to describe TPD experiments from a supported Ni catalyst.[8] Furthermore, such an effort should include coverage effects. Another challenge for mechanism generation and microkinetic modeling for CO_2 methanation on industrial catalysts is the influence of basic sites on the support for *e.g.* Ni/γ-Al_2O_3 catalysts.[8,65,96] Basic supports lead to more active Ni catalysts because the support participates in the activation of CO_2 by providing lower energy pathways at the metal/support interface[16,17] and should, therefore, be included for these systems.

The combination of linear scaling and BEP relations is commonly used to screen the activity of catalysts over the whole range of transition metals with an assumed microkinetic model, including CO^* methanation.[33,34,93,97] For the screening procedure, the binding energy of the descriptor species is changed by a few eV to move across the various transition metals. Simultaneously, the structure of the underlying microkinetic model is assumed to be static, is often derived from the knowledge for one particular metal/facet, and a single pathway is assumed. In a similar approach, Wolcott et al.[95] screened catalysts with the DRC method and observed that the rate-controlling transition state is constant in the range of a few eV. Within this study, we showed that within a few meV (i) the mechanism changes significantly, (ii) the activity varies over several orders of magnitude, (iii) the DRC is far from constant, and (iv) global and local rate-controlling parameters are completely different. Consequently, the conclusions drawn from the screening for the most active materials might be incorrect because of the simplified microkinetics. Nonetheless, the usage of these screening techniques has boosted catalyst development and advanced our understanding of several important reactions. Including automated mechanism generation into the catalyst screening procedure with correlated uncertainties is not only beneficial, but rather necessary to truly advance the predictive power of the LS and BEP relations and to determine the most active and selective materials. Although the purpose of this work is emphatically not catalyst screening, the results suggest at a nickel-like alloy that has a slightly reduced binding energy for H^* and slightly increased binding energy for adsorbates that bind through oxygen, relative to Ni(111), will offer superior production rates for CH_4.

Finally, it is worth emphasizing the computational efficiency of this approach. It took approximately 24 CPU-hours to generate all 5,000 mechanisms. The various sensitivity analyses took an additional ~300 CPU-hours. A single CINEB calculation, in contrast, required approximately 1,300 CPU-hours on the same architecture. In other words, the current approach built and analyzed 5,000 mechanisms in one-fifth of the time required to perform a single transition state calculation.

Conclusion

The present work presents the first application of automatic mechanism generation for CO_2 hydrogenation to CH_4 on Ni(111) using the open-source automated reaction generation software RMG.[39,40,43,54] Uncertainties in the model generating parameters, such as adsorbate binding energies and activation energies, were explored in a systematic manner that is consistent with the underlying correlation. Moreover, this is the first work including correlated parametric uncertainty in a rate-based automated mechanism generation procedure. RMG was capable of discovering a vast reaction network including up to C_6 chemistry, but the main path is the methanation of CO_2 via various routes. The global uncertainty analysis reveals that it is necessary to consider the uncertainties in the model input parameters to discover all possible species and reactions.

CO_2 methanation simulations with all discovered mechanisms in a PFR model shows a vast spread of results. This allows various interpretations of the Ni(111) facet activity within the uncertainty of DFT functionals and it is even possible to reach opposite conclusions. From all mechanisms, we discovered sets of parameters that describe our experimental results from Ni/SiO_2 catalyst with a remarkable accuracy without parameter optimization.

In combination with the global sensitivity analysis, it was possible to determine which factors control the activity of Ni(111) and to derive a most likely methanation mechanism, which is a combination of the redox and carboxyl pathway. The only relevant conversion from CO^* to CH_4 occurs via HCO^* and this reaction together with the thermochemistry of H^* and O^* determines the (in)activity of Ni(111).

The analysis reveals that results from the degree of rate control approach is highly sensitive to model uncertainty, and that small changes to the parameters can result in completely different degrees of rate control. A more useful approach is to perform the degree of rate control over the entire uncertainty range, since it quantifies which factors truly control the activity, and thus which parameters need to be refined the most. This new methodology is computationally efficient and can be applied to arbitrary systems in heterogeneous catalysis.

Acknowledgement

BK gratefully acknowledges financial support from the NaWuReT (ProcessNet, DECHEMA) for a virtual research collaboration with CFG in the fall of 2020. BK and TT acknowledge financial support from the Deutsche Forschungsgemeinschaft (DFG, German Research Foundation), project number: 290019031. KS, EM, KB, RHW, and CFG gratefully acknowledge support by the U.S. Department of Energy, Office of Science, Basic Energy Sciences, under Award #0000232253, as part of the Computational Chemical Sciences Program. BK and CFG thank Habib Najm and Judit Zádor for helpful discussions on sensitivity analysis. Sandia National Laboratories is a multimission laboratory managed and operated by National Technology and Engineering Solutions of Sandia, LLC, a wholly owned subsidiary of Honeywell International Inc., for the U.S. Department of Energy's National Nuclear Security Administration under contract DE-NA0003525.

Supporting Information Available

Supporting information to this article is available online.

Detailed information on the theoretical methods; DFT/CINEB results; additional simulation results; DRC and concentration heatmaps; DRC scatter plots; microkinetic model of the best case.

References

(1) Götz, M.; Lefebvre, J.; Mörs, F.; McDaniel Koch, A.; Graf, F.; Bajohr, S.; Reimert, R.; Kolb, T. Renewable Power-to-Gas: A Technological and Economic Review. *Renewable Energy* **2016**, *85*, 1371–1390.

(2) Vogt, C.; Monai, M.; Kramer, G. J.; Weckhuysen, B. M. The Renaissance of the Sabatier Reaction and its Applications on Earth and in Space. *Nat. Catal.* **2019**, *2*, 188–197.

(3) Kalz, K. F.; Kraehnert, R.; Dvoyashkin, M.; Dittmeyer, R.; Gläser, R.; Krewer, U.; Reuter, K.; Grunwaldt, J.-D. Future Challenges in Heterogeneous Catalysis: Understanding Catalysts under Dynamic Reaction Conditions. *ChemCatChem* **2017**, *9*, 17–29.

(4) Kreitz, B.; Wehinger, G. D.; Turek, T. Dynamic Simulation of the CO_2 Methanation in a Micro-Structured Fixed-Bed Reactor. *Chem. Eng. Sci.* **2019**, *195*, 541–552.

(5) Fischer, K. L.; Langer, M. R.; Freund, H. Dynamic Carbon Dioxide Methanation in a Wall-Cooled Fixed Bed Reactor: Comparative Evaluation of Reactor Models. *Ind. Eng. Chem. Res.* **2019**, *58*, 19406–19420.

(6) Kreitz, B.; Brauns, J.; Wehinger, G. D.; Turek, T. Modeling the Dynamic Power–to–Gas Process: Coupling Electrolysis with CO_2 Methanation. *Chem. Ing. Tech.* **2020**, *92*, 1992–1997.

(7) Gao, J.; Liu, Q.; Gu, F.; Liu, B.; Zhong, Z.; Su, F. Recent Advances in Methanation Catalysts for the Production of Synthetic Natural Gas. *RSC Adv.* **2015**, *5*, 22759–22776.

(8) Kreitz, B.; Wehinger, G. D.; Goldsmith, C. F.; Turek, T. Microkinetic Modeling of the CO_2 Desorption from Supported Multifaceted Ni Catalysts. *J. Phys. Chem. C* **2021**, *125*, 2984–3000.

(9) Vogt, C.; Groeneveld, E.; Kamsma, G.; Nachtegaal, M.; Lu, L.; Kiely, C. J.; Berben, P. H.; Meirer, F.; Weckhuysen, B. M. Unravelling Structure Sensitivity in CO_2 Hydrogenation over Nickel. *Nat. Catal.* **2018**, *1*, 127–134.

(10) Vogt, C.; Monai, M.; Sterk, E. B.; Palle, J.; Melcherts, A. E. M.; Zijlstra, B.; Groeneveld, E.; Berben, P. H.; Boereboom, J. M.; Hensen, E. J. M.; Meirer, F.; Filot, I. A. W.; Weckhuysen, B. M. Understanding Carbon Dioxide Activation and Carbon-Carbon Coupling over Nickel. *Nat. Commun.* **2019**, *10*, 5330.

(11) Beierlein, D.; Häussermann, D.; Pfeifer, M.; Schwarz, T.; Stöwe, K.; Traa, Y.; Klemm, E. Is the CO_2 Methanation on Highly Loaded Ni-Al_2O_3 Catalysts Really Structure-Sensitive? *Appl. Catal., B* **2019**, *247*, 200–219.

(12) Lozano-Reis, P.; Prats, H.; Gamallo, P.; Illas, F.; Sayós, R. Multiscale Study of the Mechanism of Catalytic CO_2 Hydrogenation: Role of the Ni(111) Facets. *ACS Catal.* **2020**, *10*, 8077–8089.

(13) Heine, C.; Lechner, B. A. J.; Bluhm, H.; Salmeron, M. Recycling of CO_2: Probing the Chemical State of the Ni(111) Surface during the Methanation Reaction with Ambient-Pressure X-Ray Photoelectron Spectroscopy. *J. Am. Chem. Soc.* **2016**, *138*, 13246–13252.

(14) Ren, J.; Guo, H.; Yang, J.; Qin, Z.; Lin, J.; Li, Z. Insights Into the Mechanisms of CO_2 Methanation on Ni(111) Surfaces by Density Functional Theory. *Appl. Surf. Sci.* **2015**, *351*, 504–516.

(15) Zhou, M.; Liu, B. DFT Investigation on the Competition of the Water-Gas Shift Reaction Versus Methanation on Clean and Potassium-Modified Nickel(111) Surfaces. *ChemCatChem* **2015**, *7*, 3928–3935.

(16) Foppa, L.; Margossian, T.; Kim, S. M.; Müller, C.; Copéret, C.; Larmier, K.; Comas-Vives, A. Contrasting the Role of Ni/Al_2O_3 Interfaces in Water-Gas Shift and Dry Reforming of Methane. *J. Am. Chem. Soc.* **2017**, *139*, 17128–17139.

(17) Silaghi, M.-C.; Comas-Vives, A.; Copéret, C. CO_2 Activation on Ni/γ-Al_2O_3 Catalysts by First-Principles Calculations: From Ideal Surfaces to Supported Nanoparticles. *ACS Catal.* **2016**, *6*, 4501–4505.

(18) Andersson, M. P.; Abild-Pedersen, F.; Remediakis, I. N.; Bligaard, T.; Jones, G.; Engbæk, J.; Lytken, O.; Horch, S.; Nielsen, J. H.; Sehested, J. Structure Sensitivity of the Methanation Reaction: H_2-Induced CO Dissociation on Nickel Surfaces. *J. Catal.* **2008**, *255*, 6–19.

(19) Catapan, R. C.; Oliveira, A. A. M.; Chen, Y.; Vlachos, D. G. DFT Study of the Water–Gas Shift Reaction and Coke Formation on Ni(111) and Ni(211) Surfaces. *J. Phys. Chem. C* **2012**, *116*, 20281–20291.

(20) de Carvalho, T. P.; Catapan, R. C.; Oliveira, A. A. M.; Vlachos, D. G. Microkinetic Modeling and Reduced Rate Expression of the Water–Gas Shift Reaction on Nickel. *Ind. Eng. Chem. Res.* **2018**, *57*, 10269–10280.

(21) Zhang, M.; Zijlstra, B.; Filot, I. A. W.; Li, F.; Wang, H.; Li, J.; Hensen, E. J. M. A Theoretical Study of the Reverse Water–Gas Shift Reaction on Ni(111) and Ni(311) Surfaces. *Can. J. Chem. Eng.* **2020**, *98*, 740–748.

(22) Maulana, A. L.; Putra, R. I. D.; Saputro, A. G.; Agusta, M. K.; Nugraha,; Dipojono, H. K. DFT and Microkinetic Investigation of Methanol Synthesis via CO_2 Hydrogenation on Ni(111)-Based Surfaces. *Phys. Chem. Chem. Phys.* **2019**, *21*, 20276–20286.

(23) Peng, G.; Sibener, S. J.; Schatz, G. C.; Ceyer, S. T.; Mavrikakis, M. CO_2 Hydrogenation to Formic Acid on Ni(111). *J. Phys. Chem. C* **2012**, *116*, 3001–3006.

(24) Banerjee, A.; Navarro, V.; Frenken, J. W. M.; van Bavel, A. P.; Kuipers, H. P. C. E.; Saeys, M. Shape and Size of Cobalt Nanoislands Formed Spontaneously on Cobalt Terraces during Fischer-Tropsch Synthesis. *J. Phys. Chem. Lett.* **2016**, *7*, 1996–2001.

(25) Grabow, L. C.; Mavrikakis, M. Mechanism of Methanol Synthesis on Cu through CO_2 and CO Hydrogenation. *ACS Catal.* **2011**, *1*, 365–384.

(26) Weststrate, C. J. K.-J.; Sharma, D.; Garcia Rodriguez, D.; Gleeson, M. A.; Fredriksson, H. O. A.; Niemantsverdriet, J. W. H. Mechanistic Insight Into Carbon-Carbon Bond Formation on Cobalt Under Simulated Fischer-Tropsch Synthesis Conditions. *Nat. Commun.* **2020**, *11*, 750.

(27) Gunasooriya, G. T. K. K.; van Bavel, A. P.; Kuipers, H. P. C. E.; Saeys, M. Key Role of Surface Hydroxyl Groups in C–O Activation during Fischer–Tropsch Synthesis. *ACS Catal.* **2016**, *6*, 3660–3664.

(28) Studt, F.; Abild-Pedersen, F.; Wu, Q.; Jensen, A. D.; Temel, B.; Grunwaldt, J.-D.; Nørskov, J. K. CO Hydrogenation to Methanol on Cu–Ni Catalysts: Theory and Experiment. *J. Catal.* **2012**, *293*, 51–60.

(29) Margraf, J. T.; Reuter, K. Systematic Enumeration of Elementary Reaction Steps in Surface Catalysis. *ACS Omega* **2019**, *4*, 3370–3379.

(30) Bruix, A.; Margraf, J. T.; Andersen, M.; Reuter, K. First-Principles-Based Multiscale Modelling of Heterogeneous Catalysis. *Nat. Catal.* **2019**, *2*, 659–670.

(31) Abild-Pedersen, F.; Greeley, J.; Studt, F.; Rossmeisl, J.; Munter, T. R.; Moses, P. G.; Skúlason, E.; Bligaard, T.; Nørskov, J. K. Scaling Properties of Adsorption Energies for

Hydrogen-Containing Molecules on Transition-Metal Surfaces. *Phys. Rev. Lett.* **2007**, *99*, 016105.

(32) Sutton, J. E.; Vlachos, D. G. Building Large Microkinetic Models With First-Principles' Accuracy at Reduced Computational Cost. *Chem. Eng. Sci.* **2015**, *121*, 190–199.

(33) Nørskov, J. K.; Bligaard, T.; Rossmeisl, J.; Christensen, C. H. Towards the Computational Design of Solid Catalysts. *Nat. Chem.* **2009**, *1*, 37–46.

(34) Nørskov, J. K.; Abild-Pedersen, F.; Studt, F.; Bligaard, T. Density Functional Theory in Surface Chemistry and Catalysis. *Proc. Natl. Acad. Sci. U. S. A.* **2011**, *108*, 937–943.

(35) Vernuccio, S.; Broadbelt, L. J. Discerning complex reaction networks using automated generators. *AIChE J.* **2019**, *65*, 17.

(36) Rangarajan, S.; Bhan, A.; Daoutidis, P. Identification and Analysis of Synthesis Routes in Complex Catalytic Reaction Networks for Biomass Upgrading. *Appl. Catal.,B* **2014**, *145*, 149–160.

(37) Rangarajan, S.; R. O. Brydon, R.; Bhan, A.; Daoutidis, P. Automated Identification of Energetically Feasible Mechanisms of Complex Reaction Networks in Heterogeneous Catalysis: Application to Glycerol Conversion on Transition Metals. *Green Chem.* **2014**, *16*, 813–823.

(38) Zhang, S.; Broadbelt, L. J.; Androulakis, I. P.; Ierapetritou, M. G. Reactive Flow Simulation Based on the Integration of Automated Mechanism Generation and On-the-Fly Reduction. *Energy Fuels* **2014**, *28*, 4801–4811.

(39) Gao, C. W.; Allen, J. W.; Green, W. H.; West, R. H. Reaction Mechanism Generator: Automatic Construction of Chemical Kinetic Mechanisms. *Comput. Phys. Commun.* **2016**, *203*, 212–225.

(40) Goldsmith, C. F.; West, R. H. Automatic Generation of Microkinetic Mechanisms for Heterogeneous Catalysis. *J. Phys. Chem. C* **2017**, *121*, 9970–9981.

(41) Mazeau, E.; Satpute, P.; Blondal, K.; Goldsmith, F.; West, R. *Automated Mechanism Generation Using Linear Scaling Relationships and Sensitivity Analyses Applied to Catalytic Partial Oxidation of Methane*; 2021.

(42) Blondal, K.; Jelic, J.; Mazeau, E.; Studt, F.; West, R. H.; Goldsmith, C. F. Computer-Generated Kinetics for Coupled Heterogeneous/Homogeneous Systems: A Case Study in Catalytic Combustion of Methane on Platinum. *Ind. Eng. Chem. Res.* **2019**, *58*, 17682–17691.

(43) Green, W. H.; West, R. H. RMG - Reaction Mechanism Generator. `https://rmg.mit.edu/`, 2021; Version 3.0.

(44) Döpking, S.; Plaisance, C. P.; Strobusch, D.; Reuter, K.; Scheurer, C.; Matera, S. Addressing Global Uncertainty and Sensitivity in First-Principles Based Microkinetic Models by an Adaptive Sparse Grid Approach. *J. Chem. Phys.* **2018**, *148*, 034102.

(45) Sutton, J. E.; Vlachos, D. G. Effect of Errors in Linear Scaling Relations and Brønsted–Evans–Polanyi Relations on Activity and Selectivity Maps. *J. Catal.* **2016**, *338*, 273–283.

(46) Matera, S.; Schneider, W. F.; Heyden, A.; Savara, A. Progress in Accurate Chemical Kinetic Modeling, Simulations, and Parameter Estimation for Heterogeneous Catalysis. *ACS Catal.* **2019**, *9*, 6624–6647.

(47) Ulissi, Z. W.; Medford, A. J.; Bligaard, T.; Nørskov, J. K. To Address Surface Reaction Network Complexity Using Scaling Relations Machine Learning and DFT Calculations. *Nat. Commun.* **2017**, *8*, 14621.

(48) Wellendorff, J.; Lundgaard, K. T.; Møgelhøj, A.; Petzold, V.; Landis, D. D.; Nørskov, J. K.; Bligaard, T.; Jacobsen, K. W. Density Functionals for Surface Science: Exchange-Correlation Model Development with Bayesian Error Estimation. *Phys. Rev. B* **2012**, *85*, 316.

(49) Medford, A. J.; Wellendorff, J.; Vojvodic, A.; Studt, F.; Abild-Pedersen, F.; Jacobsen, K. W.; Bligaard, T.; Nørskov, J. K. Catalysis. Assessing the Reliability of Calculated Catalytic Ammonia Synthesis Rates. *Science* **2014**, *345*, 197–200.

(50) Bligaard, T.; Nørskov, J. K.; Dahl, S.; Matthiesen, J.; Christensen, C. H.; Sehested, J. The Brønsted–Evans–Polanyi Relation and the Volcano Curve in Heterogeneous Catalysis. *J. Catal.* **2004**, *224*, 206–217.

(51) Ulissi, Z.; Prasad, V.; Vlachos, D. G. Effect of Multiscale Model Uncertainty on Identification of Pptimal Catalyst Properties. *J. Catal.* **2011**, *281*, 339–344.

(52) Wang, B.; Chen, S.; Zhang, J.; Li, S.; Yang, B. Propagating DFT Uncertainty to Mechanism Determination, Degree of Rate Control, and Coverage Analysis: The Kinetics of Dry Reforming of Methane. *J. Phys. Chem. C* **2019**, *123*, 30389–30397.

(53) Gu, T.; Wang, B.; Chen, S.; Yang, B. Automated Generation and Analysis of the Complex Catalytic Reaction Network of Ethanol Synthesis from Syngas on Rh(111). *ACS Catal.* **2020**, *10*, 6346–6355.

(54) Liu, M.; Dana, A. G.; Johnson, M.; Goldman, M.; Jocher, A.; Payne, A. M.; Grambow, C.; Han, K.; Yee, N. W.-W.; Mazeau, E.; Blondal, K.; West, R.; Goldsmith, F.; Green, W. H. Reaction Mechanism Generator v3.0: Advances in Automatic Mechanism Generation. **2020**,

(55) Susnow, R. G.; Dean, A. M.; Green, W. H.; Peczak, P.; Broadbelt, L. J. Rate-Based Construction of Kinetic Models for Complex Systems. *J.Phys. Chem. A* **1997**, *101*, 3731–3740.

(56) Goldsmith, C. F. Estimating the Thermochemistry of Adsorbates Based Upon Gas-Phase Properties. *Top. Catal.* **2012**, *55*, 366–375.

(57) Hammer, B.; Hansen, L. B.; Nørskov, J. K. Improved Adsorption Energetics Within Density-Functional Theory Using Revised Perdew-Burke-Ernzerhof Functionals. *Phys. Rev. B* **1999**, *59*, 7413–7421.

(58) Kresse, G.; Furthmüller, J. Efficient Iterative Schemes for ab Initio Total-Energy Calculations Using a Plane-Wave Basis Set. *Phys. Rev. B: Condens. Matter Mater. Phys.* **1996**, *54*, 11169–11186.

(59) Kresse, G.; Furthmüller, J. Efficiency of Ab-Initio Total Energy Calculations for Metals and Semiconductors Using a Plane-Wave Basis Set. *Comput. Mater. Sci.* **1996**, *6*, 15–50.

(60) Grimme, S. Semiempirical GGA-Type Density Functional Constructed with a Long-Range Dispersion Correction. *J. Comput. Chem.* **2006**, *27*, 1787–1799.

(61) Delgado, K.; Maier, L.; Tischer, S.; Zellner, A.; Stotz, H.; Deutschmann, O. Surface Reaction Kinetics of Steam- and CO_2-Reforming as Well as Oxidation of Methane over Nickel-Based Catalysts. *Catalysts* **2015**, *5*, 871–904.

(62) Sutton, J. E.; Panagiotopoulou, P.; Verykios, X. E.; Vlachos, D. G. Combined DFT, Microkinetic, and Experimental Study of Ethanol Steam Reforming on Pt. *J. Phys. Chem. C* **2013**, *117*, 4691–4706.

(63) Henkelman, G.; Uberuaga, B. P.; Jónsson, H. A Climbing Image Nudged Elastic Band Method for Finding Saddle Points and Minimum Energy Paths. *J. Chem. Phys.* **2000**, *113*, 9901–9904.

(64) Kreitz, B.; Martínez Arias, A.; Martin, J.; Weber, A. P.; Turek, T. Spray-Dried Ni Catalysts with Tailored Properties for CO_2 Methanation. *Catalysts* **2020**, *10*, 1410.

(65) Pan, Q.; Peng, J.; Sun, T.; Wang, S.; Wang, S. Insight Into the Reaction Route of CO_2 Methanation: Promotion Effect of Medium Basic Sites. *Catal. Commun.* **2014**, *45*, 74–78.

(66) Friedland, J.; Kreitz, B.; Grimm, H.; Turek, T.; Güttel, R. Measuring Adsorption Capacity of Supported Catalysts with a Novel Quasi-Continuous Pulse Chemisorption Method. *ChemCatChem* **2020**, *12*, 4373–4386.

(67) Goodwin, D. G.; Speth, R. L.; Moffat, H. K.; Weber, B. W. Cantera: An Object-Oriented Software Toolkit for Chemical Kinetics, Thermodynamics, and Transport Processes. `https://www.cantera.org`, 2018; Version 2.4.0.

(68) Gao, C. W.; Liu, M.; Green, W. H. Uncertainty Analysis of Correlated Parameters in Automated Reaction Mechanism Generation. *Int. J. Chem. Kinet.* **2020**, *52*, 266–282.

(69) Ruscic, B.; Pinzon, R. E.; Morton, M. L.; von Laszevski, G.; Bittner, S. J.; Nijsure, S. G.; Amin, K. A.; Minkoff, M.; Wagner, A. F. Introduction to Active Thermochemical Tables: Several "Key" Enthalpies of Formation Revisited. *J. Phys. Chem. A* **2004**, *108*, 9979–9997.

(70) Ruscic, B.; Bross, D. H. `https://atct.anl.gov`, Active Thermochemical Tables (ATcT) Values Based on ver. 1.122g of the Thermochemical Network.

(71) Prager, J.; Najm, H. N.; Sargsyan, K.; Safta, C.; Pitz, W. J. Uncertainty Quantification of Reaction Mechanisms Accounting for Correlations Introduced by Rate Rules and Fitted Arrhenius Parameters. *Combust. Flame* **2013**, *160*, 1583–1593.

(72) Sutton, J. E.; Vlachos, D. G. Ethanol Activation on Closed-Packed Surfaces. *Ind. Eng. Chem. Res.* **2015**, *54*, 4213–4225.

(73) Sobol', I. On the Distribution of Points in a Cube and the Approximate Evaluation

of Integrals. *USSR Computational Mathematics and Mathematical Physics* **1967**, *7*, 86–112.

(74) Paszke, A. *et al.* In *Advances in Neural Information Processing Systems 32*; Wallach, H., Larochelle, H., Beygelzimer, A., d'Alché-Buc, F., Fox, E., Garnett, R., Eds.; Curran Associates, Inc., 2019; pp 8024–8035.

(75) Saltelli, A.; Tarantola, S.; Campolongo, F.; Ratto, M. *Sensitivity Analysis in Practice: A Guide to Assessing Scientific Models*; Wiley Online Library, 2004; Vol. 1.

(76) Debusschere, B.; Najm, H.; Pébay, P.; Knio, O.; Ghanem, R.; Le Maître, O. Numerical Challenges in the Use of Polynomial Chaos Representations for Stochastic Processes. *SIAM J. Sci. Comput.* **2004**, *26*, 698–719.

(77) Debusschere, B.; Sargsyan, K.; Safta, C.; Chowdhary, K. In *Handbook of Uncertainty Quantification*; Ghanem, R., Higdon, D., Owhadi, H., Eds.; Springer, 2017; pp 1807–1827.

(78) Crestaux, T.; Le Maître, O.; Martinez, J. Polynomial Chaos Expansion for Sensitivity Analysis. *Reliab. Eng. Syst. Safety* **2009**, *94*, 1161–1172.

(79) Turányi, T.; Tomlin, A. S. *Analysis of Kinetic Reaction Mechanisms*; Springer Berlin Heidelberg: Berlin, Heidelberg, 2014.

(80) Campbell, C. T. Finding the Rate-Determining Step in a Mechanism. *J. Catal.* **2001**, *204*, 520–524.

(81) Stegelmann, C.; Andreasen, A.; Campbell, C. T. Degree of Rate Control: How Much the Energies of Intermediates and Transition States Control Rates. *J. Am. Chem. Soc.* **2009**, *131*, 8077–8082.

(82) Campbell, C. T. The Degree of Rate Control: A Powerful Tool for Catalysis Research. *ACS Catal.* **2017**, *7*, 2770–2779.

(83) Zádor, J.; Zsély, I. G.; Turányi, T.; Ratto, M.; Tarantola, S.; Saltelli, A. Local and Global Uncertainty Analyses of a Methane Flame Model. *J. Phys. Chem. A* **2005**, *109*, 9795–9807.

(84) Kreitz, B.; Sargsyan, K.; Mazeau, E. J.; Blöndal, K.; West, R. H.; Wehinger, G. D.; Turek, T.; Goldsmith, C. F. Data for Quantifying the Impact of Parametric Uncertainty on Automatic Mechanism Generation for CO_2 Hydrogenation on Ni(111). 2021; `https://doi.org/10.5281/zenodo.4662852`.

(85) Abelló, S.; Berrueco, C.; Montané, D. High-Loaded Nickel–Alumina Catalyst for Direct CO_2 Hydrogenation Into Synthetic Natural Gas (SNG). *Fuel* **2013**, *113*, 598–609.

(86) Koschany, F.; Schlereth, D.; Hinrichsen, O. On the Kinetics of the Methanation of Carbon Dioxide on Coprecipitated $NiAl(O)_x$. *Appl. Catal., B* **2016**, *181*, 504–516.

(87) Aziz, M.; Jalil, A. A.; Triwahyono, S.; Mukti, R. R.; Taufiq-Yap, Y. H.; Sazegar, M. R. Highly Active Ni-promoted Mesostructured Silica Nanoparticles for CO_2 Methanation. *Appl. Catal., B* **2014**, *147*, 359–368.

(88) Vrijburg, W. L.; van Helden, J. W. A.; van Hoof, A. J. F.; Friedrich, H.; Groeneveld, E.; Pidko, E. A.; Hensen, E. J. M. Tunable Colloidal Ni Nanoparticles Confined and Redistributed in Mesoporous Silica for CO_2 Methanation. *Catal. Sci. Technol.* **2019**, *9*, 2578–2591.

(89) Mhadeshwar, A. B.; Wang, H.; Vlachos, D. G. Thermodynamic Consistency in Microkinetic Development of Surface Reaction Mechanisms. *J. Phys. Chem. B* **2003**, *107*, 12721–12733.

(90) Salciccioli, M.; Stamatakis, M.; Caratzoulas, S.; Vlachos, D. G. A Review of Multiscale Modeling of Metal-Catalyzed Reactions: Mechanism Development for Complexity and Emergent Behavior. *Chem. Eng. Sci.* **2011**, *66*, 4319–4355.

(91) Vesselli, E.; Rizzi, M.; de Rogatis, L.; Ding, X.; Baraldi, A.; Comelli, G.; Savio, L.; Vattuone, L.; Rocca, M.; Fornasiero, P.; Baldereschi, A.; Peressi, M. Hydrogen-Assisted Transformation of CO_2 on Nickel: The Role of Formate and Carbon Monoxide. *J. Phys. Chem. Lett.* **2009**, *1*, 402–406.

(92) Galhardo, T. S.; Braga, A. H.; Arpini, B. H.; Szanyi, J.; Gonçalves, R. V.; Zornio, B. F.; Miranda, C. R.; Rossi, L. M. Optimizing Active Sites for High CO Selectivity during CO_2 Hydrogenation over Supported Nickel Catalysts. *J. Am. Chem. Soc.* **2021**,

(93) Lausche, A. C.; Medford, A. J.; Khan, T. S.; Xu, Y.; Bligaard, T.; Abild-Pedersen, F.; Nørskov, J. K.; Studt, F. On the Effect of Coverage-Dependent Adsorbate–Adsorbate Interactions for CO Methanation on Transition Metal Surfaces. *J. Catal.* **2013**, *307*, 275–282.

(94) Grabow, L. C.; Hvolbæk, B.; Nørskov, J. K. Understanding Trends in Catalytic Activity: The Effect of Adsorbate–Adsorbate Interactions for CO Oxidation Over Transition Metals. *Top. Catal.* **2010**, *53*, 298–310.

(95) Wolcott, C. A.; Medford, A. J.; Studt, F.; Campbell, C. T. Degree of Rate Control Approach to Computational Catalyst Screening. *J. Catal.* **2015**, *330*, 197–207.

(96) Ewald, S.; Hinrichsen, O. On the Interaction of CO_2 with Ni-Al Catalysts. *Appl. Catal., A* **2019**, *580*, 71–80.

(97) Jones, G.; Bligaard, T.; Abild-Pedersen, F.; Nørskov, J. K. Using Scaling Relations to Understand Trends in the Catalytic Activity of Transition Metals. *J. Phys.: Condens. Matter* **2008**, *20*, 064239.

Graphical TOC Entry

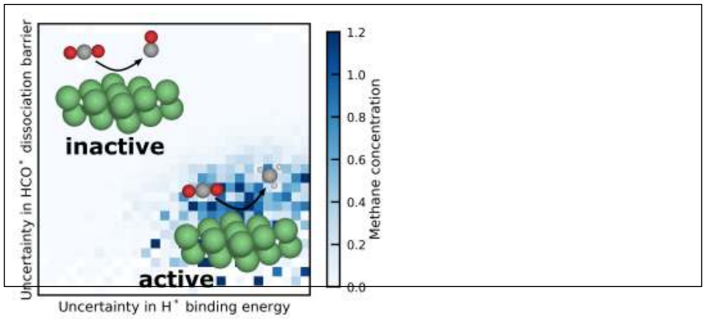
inactive
active
Uncertainty in HCO* dissociation barrier
Uncertainty in H* binding energy
Methane concentration
1.2
1.0
0.8
0.6
0.4
0.2
0.0